Travertine precipitation in the Paleoproterozoic Kuetsjärvi Sedimentary Formation, Pechenga Greenstone Belt, NE Fennoscandian Shield

Salminen, P.E.[a*], Brasier, A.T.[b], Karhu, J.A[a], Melezhik, V.A.[c,d]

a Department of Geosciences and Geography, P.O. Box 64 (Gustaf Hällsrömin katu 2a), 00014 University of Helsinki, Finland

b Department of Geology and Petroleum Geology, Meston Building, University of Aberdeen, Scotland. AB24 3UE

c Geological Survey of Norway, Leiv Eriksson vei 39, N-4791 Trondheim, Norway

*Corresponding author, Tel. +358 02941 50834, fax: +358 02941 50826, E-mail: paula.salminen@alumni.helsinki.fi

Abstract

Precambrian travertines, tufas and speleothems either formed rarely or they have not been identified in previous studies. In the absence of high pCO_2 soils in Paleoproterozoic, karst solution and speleothem formation occurred by processes distinct from those commonly found in present-day low temperature karst environments. However, the high pCO_2 atmosphere could itself have encouraged karst formation. The Paleoproterozoic Kuetsjärvi Sedimentary Formation of the Pechenga Greenstone Belt, NW Russia, includes abundant terrestrial carbonate precipitates. These precipitates were sampled from a drillcore representing a complete section of the ca. 120-m-thick formation and were investigated for C and O isotopes, acid-soluble elemental contents and petrography. The newly obtained results were used to constrain the origins of the precipitates and to illuminate different terrestrial carbonate types. The investigated drillcore includes abundant small-scale cavities and veins, which are commonly filled with dolomite and quartz. Dolomite crusts are found both in the cavities and on

bedding/erosional surfaces. Dolomite cements coat uneven surfaces and surficial rock fragments. The surficial dolomite crusts form distinct and discrete layers, whereas the cements do not. The cavity and vein fills are likely post-depositional in origin, whereasthe surficial dolomite crusts and dolomite cements are likely syn-depositional precipitates. The investigated precipitates often show $\delta^{13}C$ values lower than those reported from their host rocks, suggesting the influence of an external carbon source. Petrographic features and geochemical data suggest dissolution and precipitation of carbonate material originating from deep-sourced CO_2-bearing fluids, likely at high earth surface temperatures.

Keywords: Travertine, speleothem, carbonate, dissolution, degassing, Paleoproterozoic

1. Introduction

Reports of Precambrian travertines, tufas and speleothems are rare because they either rarely formed or have not been identified (see Brasier, 2011; Brasier et al., 2013). Identifying these deposits in drillcore can be problematic as examples may be mistaken for signs of post-depositional alteration. Distinction between travertines, tufas and speleothems is also challenging and perhaps unnecessary(e.g. Brasier, 2011; Rogerson et al., 2014).

Travertine and tufa have been classified in many ways. The word “tufa” was originally used for both volcanic ash and soft, poorly consolidated freshwater carbonate, but later “calcareous tufa” was used for freshwater carbonates (e.g. Pentecost, 1993; Pentecost and Viles, 1994). Today, many sedimentologists use “calcareous tufa” or “tufa” for the softer varieties (unsuitable for building), whereas the word “travertine” is used for harder freshwater carbonates (e.g. Pentecost and Viles, 1994). However, travertine and tufa have also been

classified according to their fabrics, morphology, geochemistry and water temperature at time of deposition (e.g. Ford and Pedley, 1996; Pentecost and Viles, 1994).

In some cases the word "travertine" is used for both thermal (above ambient) and ambient water temperature chemical carbonate precipitates, and can be divided into (i) thermal or thermogene travertines and (ii) meteogene travertines (e.g. Pentecost and Viles, 1994). Thermal travertines are normally precipitated from hot waters and their carrier CO_2 primarily originates from interaction of hot rock and CO_2-rich fluid (Pentecost and Viles, 1994). The carried CO_2 for the precipitation of meteogene travertines is derived from soils and epigean atmosphere (Pentecost and Viles, 1994).

Alternatively, the word "travertine" can be used for thermal/hydrothermal precipitates and the word "tufa" for cool/near-ambient water precipitates (e.g. Ford and Pedley, 1996; Pedley, 1990; Riding, 1991). In modern environments macrophytes can be used to distinguish between travertine and tufa: travertines lack macrophyte remains, but tufas are commonly characterized by macrophytes (e.g. Ford and Pedley, 1996). As there were no plants during Precambrian, distinguishing between travertine and tufa is difficult or even impossible (Brasier, 2011).

Modern speleothems are usually formed under high pCO_2 soils. These both provide carbonic acid for carbonate bedrock dissolution and provide a contrast with the low pCO_2 of the cave atmosphere that enables degassing of drip-waters causing carbonate mineral precipitation (e.g. Fairchild et al., 2000; Frisia and Borsato, 2010). Paleoproterozoic karst and speleothem probably formed in some other way, as there is no convincing evidence that high pCO_2 soils existed at that time (see Brasier, 2011). A high pCO_2 atmosphere could have caused carbonic acid formation and hence karst formation. Carbon dioxide degassing leading to precipitation of carbonates in high pCO_2 atmospheres is possible in certain circumstances (see Brasier,

2011). One of the most appealing explanations for Paleoproterozoic karst and speleothem formation is the common-ion effect, involving dissolution of Ca sulfate (e.g. Calaforra et al., 2008; Wigley, 1973a) or incongruent dissolution of dolomite (e.g. Wigley, 1973b). Explanations may alternatively involve deep-sourced CO_2 (e.g. Duliński et al., 1995; Pentecost and Viles, 1994), possibly connected to hydrothermal activity.

In this paper, we use the term "travertine" in a collective way for the ancient deposits we describe. The term "speleothem" is here used for cavity fills and the word "cement" for dolomites binding or coating surface rock fragments and erosional surfaces.

Carbonate rocks extremely enriched in ^{13}C were deposited world-wide during the Paleoproterozoic (ca. 2200 – 2060 Ma), marking a global positive $\delta^{13}C$ excursion recorded in sedimentary carbonates (e.g. Baker and Fallick, 1989a, 1989b; Karhu and Holland, 1996). The Kuetsjärvi Sedimentary Formation (KSF) of the Pechenga Greenstone Belt (NW Russia) records this excursion (e.g. Karhu, 1993; Karhu and Melezhik, 1992; Melezhik et al., 2005, Salminen et al., 2013a). The KSF exposures and cores are excellently preserved, and provide an opportunity for studying Paleoproterozoic carbonate rock environments and precipitation processes. In addition to stratified dolostone and limestone, hot-spring associated travertines have previously been interpreted from the KSF (Melezhik and Fallick, 2001). Carbonates associated with dissolution surfaces and small-scale cavities (epikarst) have also been found in the KSF (Melezhik et al., 2004), along with calcrete (caliche) and dolocrete (e.g. Melezhik et al. 2004; Melezhik and Fallick, 2003). These calcrete and dolocrete instances were interpreted to have formed by capillary rise and evaporation (Melezhik et al., 2004; Melezhik and Fallick, 2003). Moreover, Melezhik and Fallick (2005) reported probable $CaSO_4$ pseudomorphs in the KSF sabkha- or playa- carbonates.

In this study, discrete morphologies of carbonate precipitates were investigated from a drillcore of the KSF. These included dolomite crusts, dolomite cements, and carbonate fills in small-scale cavities and veins. A detailed petrographic picture of the precipitates was constructed. Several samples were analyzed for the isotope composition of C and O and acid-soluble abundances of selected elements. Results were compared to those of the more common stratified dolostone and limestone rocks from the same drillcore (Salminen et al., 2013a).

The goals of this research were to (1) identify and characterize different kinds of Precambrian terrestrial carbonates, (2) decipher the origins of the investigated carbonate precipitates, and (3) provide additional information on the depositional setting of the KSF.

2. Geological background

2.1 Geological setting

This investigation is based on the samples from Core 5A, which was drilled by ICDP (International Scientific Continental Drilling Program) FAR-DEEP (Fennoscandia Arctic Russia – Drilling Early Earth Project) from the KSF of the Pechenga Greenstone Belt, NW Russia (**Fig. 1**). The geological setting of the core has previously been described by Salminen et al. (2013a, 2013b) and is briefly summarized below.

(Approximate location of Figure 1.)

The Pechenga Greenstone Belt is a section of a larger (ca. 1000 km long) belt in the north-eastern part of the Fennoscandian Shield (e.g. Melezhik and Sturt, 1994). This larger belt has

been interpreted as an intracontinental rift developed into an intercontinental rift with a subsequent aborted oceanic phase and arc-continent collision (e.g. Melezhik and Sturt, 1994). More extensive opening followed by oceanic floor subduction and arc-continent collision has also been suggested (Berthelsen and Marker, 1986). The Pechenga Greenstone Belt has been divided into the North and South Pechenga groups (e.g. Melezhik and Sturt, 1994). The KSF belongs to the North Pechenga Group, which is composed of four paired sedimentary-volcanic cycles (e.g. Melezhik and Sturt, 1994).

The Pechenga Greenstone Belt rocks underwent metamorphic alteration ranging from prehnite-pumpellyite to amphibolite facies (Petrov and Voloshina, 1995). Core 5A was drilled from biotite-actinolite phase of the greenschist facies. The KSF has also been exposed to epigenetic alteration (Melezhik, 1992).

The thickness of the KSF varies from 20 to 120 m. Its thickness in Core 5A is ca. 117 m. The KSF was deposited on a paleo-weathering crust developed on the basaltic andesites of the Ahmalahti Formation and its depositional top is defined by the first basalts of the Kuetsjärvi Volcanic Formation (Predovsky et al., 1974).

The minimum depositional age (U-Pb) of the KSF is 2058 ± 2 Ma (Melezhik et al., 2007), inferred from detrital zircons in volcaniclastic conglomerate within the Kuetsjärvi Volcanic Formation and the overlying Kolosjoki Sedimentary Formation. Martin et al. (2013) obtained a depositional age (U-Pb) of 2056.6 ± 0.8 Ma for the Kolosjoki Sedimentary Formation. A robust maximum depositional age (U-Pb) is 2505.1 ± 1.6 Ma, obtained from the Mount Generalskaya gabbronorite intrusion (Amelin et al., 1995). This intrusion is unconformably overlain by basal conglomerate of the Neverskrukk Formation, which is the lowermost formation of the North Pechenga Group.

142 Travertines of probable hot-spring origin were reported from the KSF by Melezhik and
143 Fallick (2001) and Melezhik et al. (2004). Melezhik and Fallick (2001) reported two types of
144 travertines from the KSF: (1) laminated crusts formed on a pure carbonate substrate and
145 capped by stratified, stromatolitic dolostone, and (2) small-scale mounds formed on a
146 carbonate substrate and buried under red siltstone and sandstone. In addition to travertines,
147 several other kind of subaerial exposure surfaces have been reported from the KSF (Melezhik
148 et al., 2004; Melezhik and Fallick, 2001, 2003). These include dissolution surfaces and
149 epikarst, erosional surfaces, calcrete/caliche, dolocrete, silica sinters. Dissolution surfaces and
150 epikarst included voids and small-scale cavities.

151

152 **2.2 Core 5A: lithostratigraphy and depositional setting**

153

154 A detailed lithostratigraphic description of Core 5A and an interpretation of its depositional
155 setting can be found in Salminen et al. (2013a, 2013b) with a brief summary provided below.
156 The lithostratigraphy of the core is presented in **Fig. 2**.

157 (Approximate location of Figure 2.)

158 Salminen et al. (2013b) divided the KSF in Core 5A into four informal members. From oldest
159 to youngest these are the Arkosic, Lower Dolostone, Quartzite and Upper Dolostone
160 members. A Fe-picrite dyke (ca. 5 m thick) separates the Arkosic and Lower Dolostone
161 members. Sedimentary carbonates of Drillcore 5A include micritic, sparry and stromatolitic
162 dolostone, dolarenite, micritic limestone and calcarenite. Siliciclastic rocks include arkosic to
163 quartzitic sandstone, graywacke, siltstone, shale and calcareous siliciclastic rocks (marl).

Both Lower and Upper Dolostone members show marks of erosional and dissolution processes. Dolomite crusts, surficial cements and carbonate-filled veins and small dissolution cavities are common (totaling at ca. 18 vol.%) in both of these members (see section 4; **Fig. 2**; Salminen et al., 2013a). Similar-looking dolomitic crusts and carbonate fills have previously interpreted as hot-spring associated travertines (Melezhik et al., 2004; Melezhik and Fallick, 2001).

The depositional setting of the Arkosic and Quartzite members has been assigned to delta-plain, pro-delta, deltaic environments influenced by tides (Salminen et al., 2013b). The basal part of the Quartzite member has been interpreted as a deposit from a flooding event (Salminen et al., 2013b). The Lower Dolostone member was interpreted to have deposited in a shallow-lacustrine setting and the Upper Dolostone member in a tidally influenced (hence sporadically marine) shallow-lacustrine environment (Salminen et al., 2013b).

3. Materials and methods

Samples for this study were obtained from different depth-intervals of Core 5A. All analyses were performed at the Department of Geosciences and Geography, University of Helsinki using techniques described in Salminen et al. (2013a).

Subsamples were micro-drilled with 1.0 or 1.8 mm diamond grinding bits from carbonate crusts, cements and fills. The number of subsamples from each carbonate type reflects its abundance in the core. All carbonate subsamples were analyzed for the isotope composition

of C and O. The larger subsamples (those of ca. 10 – 20 mg; drilled with the 1.8 mm bit), were also analyzed for acetic acid-soluble elements by ICP-MS (described below).

In addition, several subsamples were also obtained from the enclosing carbonate rocks, immediately over- and underlying the cavity at ca. 62.1 m. These subsamples were only analyzed for C and O isotopes, to compare/contrast with values obtained from the cavity fills.

Carbonate mineralogy (calcite or dolomite) of the larger subsamples was determined by using Mg/Ca ratios, whereas in the 1–2 mg subsamples it was determined by XRD or through a qualitative acid test (reaction with ca. 3 M HCl).

The acid-soluble Mg, Ca, Mn, Sr, Fe and Ba contents were determined using an Agilent 7500ce/cx ICP-MS. Powdered samples (9 –13 mg) were leached in 5 ml of ca. 0.5 M acetic-acid under room temperature for 16 h. The final results were calculated in relation to the acid-soluble fraction. Including the dissolution step, the average precision (1σ) was 14.6 % for the samples from the depth 79.55 – 81.50 m (excluding the sample from 81.45 m) and 7.5 % for all other samples.

The C and O isotope composition of the samples was determined using a Thermo Finnigan Delta Plus Advantage isotope ratio mass spectrometer in continuous-flow mode. The isotope compositions of ca. 125 – 170 μg powdered samples were measured on phosphoric acid liberated CO_2 gas (in 90°C for ≥1h). The C and O isotope compositions are expressed in conventional δ-notations as a per-mil difference from the international VPDB standard. An in-house dolomite quality standard indicated a long-term reproducibility (1σ) of 0.10‰ for C and 0.22‰ for O (n=59). An in-house calcite standard indicated a long-term reproducibility (1σ) of 0.08‰ for C and 0.17‰ for O (n=7).

209 Petrography and mineralogy of the carbonate precipitates were investigated in several thin
210 sections under optical microscope and by visual examination of drillcore samples. In
211 addition, selected thin sections were investigated semi-quantitatively (EDS, standardless)
212 with an electron microanalyzer (Jeol JXA-8600 superprobe, accelerating voltage 15 kV,
213 beam current 1 nA, focused beam).

214

215 ## 4. Petrography of the precipitates: description and interpretation

216

217 Core 5A contains five distinct features. These are (1) cavities, (2) veins, (3) dolomite crusts
218 filling cavities, (4) dolomite crusts precipitated on bedding/erosional surfaces, and (5)
219 dolomite cements encrusting surface rock fragments and uneven surfaces. New petrographic
220 observations and interpretations of these allow us to add substantially to the previously made
221 brief descriptions of the Core 5A rocks (Salminen et al., 2013a, b; Brasier et al., 2013). The
222 general description of the five types of precipitates is provided in Table 1 and the investigated
223 samples are described in Inline Supplementary Table 1.

224 (Approximate location of Table 1.)

225 Insert Inline Supplementary Table 1 here.

226

227 ### 4.1 Small-scale dissolution cavities (type 1)

228

229 **Description.** Dissolution cavities are found in all types of carbonate. The dolostone
230 immediately surrounding the cavity often appears recrystallized or powdery. The heights of

231 the cavities vary from a few centimeters to ca. ten centimeters. Cavities are walled with
232 rim(s) of fibrous (radiating), bladed and/or sparitic dolomite;some cavities also contain
233 calcite fills. Carbonate fills show both upwards and downwards growth. Small white
234 stalactites and stalagmites are found in places, e.g. at ca. 60.6 m. These stalactites/stalagmites
235 have concentric bedding-parallel shapes and they are composed of sparitic dolomite, walled
236 with a rim of bladed dolomite. The latest infill is usually quartz and/or dolospar (**Figs. 3-4**),
237 but in places it is quartz sandstone. Pyrite (**Fig 3b**) and dolomite ooids have also been
238 identified in some cavities.

239 Some cavities are found in possible surficial dolomite crusts. These include e.g. the cavity at
240 ca. 60.2 m. This cavity is walled with small white stalactites and stalagmites (**Fig. 5a**), similar
241 to those in the cavity at ca. 60.6 m. The remaining space of the cavity is filled with quartz and
242 patches of fibrous/sparitic dolomite. The cavity is underlain by red, beige and white, banded
243 dolomite crust and overlain by white dolomite crust and a possible silica sinter.

244 **Interpretation.** Most of the dolomite rims in the cavities are best interpreted as flowstones.
245 However, the small-scale stalactites and stalagmites probably indicate precipitation from
246 dripping water. Dolomite rims are relatively symmetrically walling the cavities. These
247 symmetrically rimmed cavities are interpreted to have been formed in dominantly phreatic
248 conditions.

249

250 (Approximate location of Figures 3-5.)

251 ### *4.1.1 Special small-scale dissolution cavity cases*
252

253 Cavities at ca. 69.6 m and 72.7 m appear somewhat different to other examples and are
254 therefore described here separately.

The dissolution cavity at 69.6 m has a complex structure, exhibiting three types of carbonate fill (**Fig. 3b**). The outermost zone includes thin laminae of white dolomite and quartz. The second zone includes yellowish, sparitic calcite, which is followed by thin laminae of white dolomite and quartz These laminae also form microstalactite-like structures. These laminae are sealed with a thin rim of fibrous dolomite. The remaining space, in the center of the cavity, is filled with quartz, dolospar and pyrite. These three fabrics represent the latest infills of the cavity. The precipitates of this cavity, like the rim of fibrous dolomite, are best interpreted to have precipitated in phreatic to vadose conditions.

The cavity at 72.7 m is filled with siliceous sparitic dolomite with quartz-filled fenestrae-like structures.(**Fig. 4b**). The morphologies of some of these fenestrae resemble sulfate pseudomorphs. The cavity ceiling is composed of white, thinly-laminated, sparitic dolomite, which also forms stalactite-like structures. Similar laminae are not found at the base of the cavity. The non-symmetrical structure of the cavity likely indicates carbonate mineral precipitation in the vadose zone.

4.2 Veins (type 2)

Description. Some structures likely represent veins, rather than filled cavities. These structures include thin (ca. 0.2–2 cm), bedding-parallel vugs (**Figs. 6a-b**). Some of these have relatively straight borders, whereas others have more curved margins. Veins are walled with rims of sparitic and bladed dolomite. the bladed dolomite shows inward growth. Quartz and/or dolospar represent the latest infills; some veins are almost entirely filled with dolospar.

277 **Interpretation.** These veins have symmetrical shapes, indicating mineral precipitation within
278 a fluid-filled space (e.g. fracture). In some veins, the flooring is thicker than the ceiling. This
279 could indicate precipitation within a gas- and fluid-filled space.

280 (Approximate location of Figure 6.)

281

282 *4.2.1 Special vein case*
283

284 A vein at ca. 53.7 m shows color and mineralogical zoning (**Fig. 6c**). This vein is larger (with
285 a height of ca. 8-9 centimeters) than other veins in the core. Its outer rim is composed of
286 white dolomite, whereas the outer rim is capped by a grayish calcitic and dolomitic layer. The
287 center of the vein is filled with orange calcite. The color zoning is more pronounced here than
288 in the cavities. Pyrite is also found in this vein. This vein may have formed during burial
289 diagenesis.

290 ### 4.3 Large cavities with dolomite crust (type 3)

291

292 **Description.** The cavities with dolomite crusts are up to ca. 20 cm thick. The flooring in
293 these cavities is thicker than the ceiling. The remaining space between the flooring and the
294 ceiling is filled with dolospar, but cavities often appear as collapsed or deformed. The
295 flooring (red, pink, beige, white, and/or gray) usually consists of banded, laminated or
296 massive dolomitic crust, which is capped with thinly-laminated gray-and-white crust. In
297 places the ceiling is composed of a dolomitic crust (white, gray or yellow) underlain by small
298 thinly-laminated gray-and-white stalactites (**Fig. 5b**), but elsewhere the crust is lacking and
299 there are only stalactites. The thinly-laminated crusts and stalactites are often deformed (**Figs.**

300 **5b**). They usually consist of alternating white and/or gray laminae of fibrous, radiating
301 dolomite (forming cones) and sparitic dolomite.

302 **Interpretation.** The cavities with dolomite crusts have probably been deposited in vadose
303 conditions. These cavities have non-symmetrical structure; the cavity flooring is thicker than
304 the ceiling coating. The basal part of the flooring is often characterized by red coloration,
305 which possibly implies deposition from an oxidizing fluid.

306

307 *4.3.1 Special large cavity with dolomite crust case*
308

309 In the cavity at ca. 31.4 m (**Fig. 5c**), the entire flooring is thinly laminated and also includes
310 dolospar and quartz filled fenestrae. The stalactites in the cavity consist of laminae of small
311 (micritic) grain size; the laminae are coloured white, gray, black or reddish (**Fig. 5c**). This
312 cavity also shows non-symmetrical structures so its fill probably precipitated in the vadose
313 zone.

314

315 **4.4 Surficial dolomite crusts (type 4)**

316

317 **General description and interpretation.** Surficial dolomite crusts were formed on bedding
318 and erosional surfaces. The crusts are composed of bedding parallel layers with uneven upper
319 surfaces and contain curved or mound-shaped laminae. Hence, the petrography and
320 morphology of these carbonate precipitates differs from normal stratified dolostone and
321 limestone of the KSF. We tentatively interpret such crusts as authigenic precipitates in

surface settings. The red coloration at the base of some crusts may imply deposition from an oxidizing fluid. Below, different types of the surficial crusts are described in more detail.

Crust at 30.3 m. One inferred surficial dolomite crust in the Upper Dolostone member (at ca. 30.3 m, **Inline Supplementary Figure 1**) shows a reddish lamination at its base, followed by beige laminated, banded or massive dolomite. This crust includes small vugs/veins, which are filled with white, grey and black sparry carbonate. The upper part of the crust has a chalky micritic appearance. The crust is capped with a rim of fibrous dolomite and quartz.

(Insert Inline Supplementary Figure 1 here)

White dolomite crusts. There are several inferred surficial dolomitic crusts composed mainly of white micritic to sparitic dolomite. The crust at ca. 68.3 m shows thin lamination (**Fig. 7**). These laminae form mound-like or oncoidal structures. These crusts are capped by a thin (<1 cm), upwards-growing rim of fibrous dolomite which is sealed with a crystalline silica sinter (**Fig. 7**). The crust at 68.3 m is overlain by a sandstone layer (**Fig. 7**).

Crust at 27.4 m. The layer at ca. 27.4 m has a complex internal structure (**Fig. 8**). Its basal part is composed of beige, laminated, micritic dolomite and contains some quartz-filled fenestrae. The basal part is overlain by a partially vuggy interval. The latter contains several small vugs, which are surrounded by beige, laminated, micritic dolomite and grayish (siliceous), structureless, sparitic dolomite. The vugs are walled by white (inner) and yellow (outer) laminae of fibrous dolomite. The remaining space in the vugs is filled with dolospar and quartz. The yellow and white laminae also form small (ca. 1 cm) mounds. The vuggy interval is sealed with a rim of white sparitic dolomite. These vugs probably formed simultaneously with the surrounding dolomites. The uneven surface of the entire layer is capped with a thin siliceous film (interpreted as a sinter or a silcrete layer). The overall structural pattern suggests a surficial dolomite crust.

(Approximate location of Figures 7-8.)

4.5 Dolomite cements (type 5)

Dolomite cements are found in the Lower Dolostone member (**Fig. 9**), chiefly at ca. 76-78 m and at 83 m. These cements consist of white feather-shaped (Figs. 9a-c) , fibrous, radial, bladed and/or sparitic dolomite. Dolomite cements do not form distinct bedding-parallel layers (in contrast to the surficial dolomite crusts), but they are found on uneven surfaces and capping or corrosively replacing sandstone fragments. Sometimes they form mound-like accumulations (**Figs. 9a-b**), which often have exhumed upper surfaces. There are also thinly-laminated cements (**Fig. 9b**). Dolomite cements usually show upward growth and appear as syn-depositional precipitates. Sometimes they are also found filling space between the sandstone fragments, showing downward growth (**Fig. 9d**); quartz or dolospar is the latest infill.

(Approximate location of Figure 9.)

Although the dolomite cements and quartz also fill void spaces between sandstone fragments, the cements are best interpreted as syn-depositional precipitates, as these precipitates are usually cementing surface rock fragments and uneven erosional surfaces.

5. Geochemical results

5.1 Electron microprobe data

Carbonate cavity fills, crusts and cements were analyzed semi-quantitatively with an electron microanalyzer to determine mineralogies. The reddish dolomite crust in the cavity flooring at ca. 81.5 m includes mainly dolomite but also calcite, quartz, talc, phlogopite, muscovite, Fe-poor chlorite, potassium feldspar and fluorapatite. Calcite was found filling the remaining space between dolomite crystals. Dolomite and minor calcite and talc were identified in the cavity at ca. 60.6 m. The quartz-filled fenestrae in the layer at ca. 72.7 m contain calcite and dolomite inclusions. Apatite and potassium feldspar were also identified in that layer. No traces of evaporite minerals were found in the investigated fenestrae. Two samples from the dolomite cements are composed of mainly dolomite with minor calcite, quartz and talc. Several minor minerals were also identified in the dolomite cements, including fluorapatite, potassium feldspar and chlorite. Possible sulfate pseudomorphs (now dolomite and calcite) were recognized in a secondary electron image (**Inline supplementary figure 2**) in the dolomite cement at ca. 76.9 m.

(Insert Inline Supplementary Figure 2 here.)

Both the electron microprobe and the microscope investigations suggest that dolomite is a primary mineral. There are no petrographic indications for dolomitization. Instead, the presence of talc could indicate that the minor calcite has been formed via de-dolomitization.

5.2 Acid-soluble elemental contents (ICP-MS)

The acid-soluble elemental contents and the Mg/Ca and Mn/Sr ratios of the carbonate fills, crusts and cements are presented in **Inline Supplementary Table 2.**

(Insert Inline Supplementary Table 2 here.)

The Mg/Ca ratios vary from 0.01 to 0.71 (n=65). Based on the Mg/Ca ratios, most of the subsamples were dolomitic. Two subsamples were calcitic. Two subsamples were mixtures of dolomite and calcite.

On the core scale, the Mn and Fe contents show subtle upwards decreasing trends. The Mn contents vary from 42 to 3900 ppm (average 640 ppm, n = 65, **Fig. 10**). The abundances of Fe range between 110 and 9600 ppm (average 1600 ppm, n = 65, **Fig.10**). The Fe concentrations correlate strongly with the Mn concentrations (r = 0.57, n = 65, **Fig. 11)**.

The Sr contents show an upwards increasing trend in the core, varying from 30 to 310 ppm (average 96 ppm, n=65, **Fig. 10**). The Sr and Mn contents do not show co-variation in the investigated carbonate precipitates (**Fig. 11**). The Ba contents do not show any clear stratigraphic trend, varying from <0.48 to 51 ppm (average 6.2 ppm, n=65, **Fig. 10**).

(Approximate location of Figures 10-11.)

5.2.1 Detailed investigations of distinct cavities and crusts

Several subsamples from the cavities at ca. 79.6 m and ca. 81.4 m were analyzed for elemental contents. In the cavity at 79.6 m *(***Fig. 12**), the highest Mn and Fe contents were obtained from a stalactite and stalagmite in the cavity center. TheFe contents show a subtle

411 upwards increase in the upper part of the cavity (in the ceiling). The Mn, Sr and Ba
412 concentrations do not exhibit any clear trends. In the cavity at 81.4 m (**Fig. 13**), the Mn and
413 Fe contents show generally upwards increasing (cyclical) trends. The Sr concentration is
414 variable, demonstrating no clear trend across the cavity, whereas the Ba content shows a
415 subtle upwards decrease.

416 (Approximate location of Figures 12-13.)

417 The vein at ca. 53.7 m shows mineralogical and color zoning. The orange infill in the center
418 is composed of calcite (Mg/Ca = 0.01), whereas the grayish rim surrounding the orange infill
419 has a mixed dolomite-calcite composition (Mg/Ca = 0.20). The white outermost rim consists
420 of dolomite (Mg/Ca = 0.64). The Mn and Ba concentrations decrease from the calcitic infill
421 towards the dolomitic rim. The highest Fe and Sr contents were obtained from the mixed
422 calcite-dolomite sample. All analyzed carbonate phases have a high Mn content (750–2700
423 ppm), whereas the Sr abundances (62–150 ppm) are higher or similar to those obtained from
424 other carbonate phases from similar depths.

425 The cavity at ca. 72.7 m includes silica filled fenestrae. As mentioned earlier, some of these
426 fenestrae morphologically resemble sulfate pseudomorphs, although no traces of sulfates
427 have been detected. High Mn (3900 ppm) and Fe (9600 ppm) contents were measured from
428 this interval. In contrast, the Sr (35 ppm) and Ba (0.82 ppm) contents are relatively low.

429

430

431 **5.3 Carbonate C and O stable isotopes**

432

The $\delta^{13}C$ and $\delta^{18}O$ values of all analyzed samples are presented in **Inline Supplementary Table 2**.

In cavity fills, crusts and cements (n = 139), the $\delta^{13}C$ values vary from 4.0 to 8.0‰ averaging at 6.8‰ (**Fig. 2**). The $\delta^{18}O$ values range from -15.1 to -8.4‰, with an average value of -12.6‰ (**Fig. 2**). In general, cavity/vein fills, surficial crusts and cements show similar variations of $\delta^{13}C$ and $\delta^{18}O$ values.

The $\delta^{13}C$ and the $\delta^{18}O$ values show moderate positive correlation (r = 0.50, n = 139, **Fig. 11**) in the carbonate fills, crusts and cements. Lower $\delta^{13}C$ values are often linked to higher Mn concentrations (**Fig. 11**). The Sr contents of the precipitates do not show correlation with the $\delta^{13}C$ or $\delta^{18}O$ values (**Fig. 11**). No significant co-variation is observed between the $\delta^{18}O$ values and the Mn contents (**Fig. 11**).

5.3.1 Detailed investigations of distinct cavities and crusts

A series of subsamples was obtained from some cavity fills. In individual crusts and cavities, the $\delta^{13}C$ and $\delta^{18}O$ values show moderate or even strong positive correlation (**Fig. 14**). Clearly decreasing $\delta^{13}C$ and $\delta^{18}O$ trends from the walls towards the centers were found in the cavities at ca. 83.0 m (**Fig. 15**) and ca. 79.6 m (**Fig. 12**). In the cavity at ca. 81.4 m (**Fig. 13**), the lowest $\delta^{13}C$ and $\delta^{18}O$ values were obtained from the upper part, which included thinly-laminated gray-and-white crust and stalactites. The $\delta^{13}C$ and $\delta^{18}O$ values show subtle upwards decreasing trends in the flooring of that cavity, followed by subtle upwards increasing $\delta^{13}C$ and $\delta^{18}O$ trends.

(Approximate location of Figures 14-15.)

The cavity fills at ca. 62.1 m show similar or lower $\delta^{13}C$ values (6.1 – 7.5‰, average 7.0‰) than those (7.3 – 7.8‰, average 7.6‰) in the carbonates enclosing the cavity (**Fig. 16**).

These rocks over- and underlying the cavity show a subtle, symmetrical decrease in their $\delta^{13}C$ values towards the cavity. The $\delta^{18}O$ values are relatively similar or slightly higher in the cavity fills (from -12.5 to -9.2‰, average -11.5‰) than in the rocks enclosing it (from -12.3 to -11.3‰, average -11.9‰) (**Fig. 16**).

(Approximate location of Figure 16.)

In the surficial crust at ca. 30.3 m (**Fig. 17**), the $\delta^{13}C$ values first show a cyclic, upwards decreasing trend (in the lowermost third of the crust), followed by a subtle tendency towards higher values. The $\delta^{18}O$ values show an increasing trend in the lowermost part of the crust, followed by a decreasing trend, and after that, variable $\delta^{18}O$ values. The upper half of the surficial dolomite crust at 68.3 m shows a small (ca. 0.5‰) increase in $\delta^{13}C$ and $\delta^{18}O$ upwards in the section (**Fig. 18**); the lower half of the crust was not investigated. These crusts at 30.22 m and 68.26 m are different in their petrography.

(Approximate location of Figures 17-18.)

Carbonates in the vein at 53.7 m vary in their $\delta^{13}C$ and $\delta^{18}O$ values. The calcitic phase (from the central orange zone of the vein) shows a $\delta^{13}C$ value of 5.2‰ and a $\delta^{18}O$ value of -12.7‰. The subsample representing a mixture of calcite and dolomite (from the grayish zone) shows a $\delta^{13}C$ value of 5.9‰ and a $\delta^{18}O$ value of -13.5‰. The dolomitic subsample (from the white zone) shows a value of 7.6‰ and a $\delta^{18}O$ value of -12.0‰. Thus, the $\delta^{13}C$ values increase from the central calcitic zone outwards, towards the dolomitic zone. In contrast, the lowest $\delta^{18}O$ value was obtained from the mixture of dolomite and calcite.

6. Discussion

480 **6.1 Petrographic aspects**

481

482 Many of the precipitates studied in Core 5A are post-depositional phases, including cavity
483 and vein fills (types 1-3). The term speleothem could be appropriate for the cavity fills.
484 Whether the waters from which they precipitated were thermal (e.g. Corbella et al., 2004;
485 Djidi et al., 2008; Dublyansky, 1995) or at ambient temperature remains to be substantiated.

486 The thinly-laminated crusts and stalactites in the type 3 cavities (**Fig. 5a, c**) are similar to
487 carbonate crusts coating modern travertines (e.g. Jones and Renaut, 2008). Moreover, some
488 of the studied carbonates (e.g. type 4) resemble the ~1.8-Ga-old Baker Lake Group laminar
489 crust travertines of Canada briefly described by Rainbird et al. (2006); those travertines are
490 associated with volcanic rocks.

491 All surficial dolomite crusts (type 3)are capped with a thin siliceous sinter or silcrete (e.g.
492 Fig. 7). This silica layer distinguishes such dolomite crust from "normal" stratified dolostones
493 of the KSF. Silica sinters in modern travertines are usually precipitated through rapid cooling
494 and/or evaporation (e.g. Jones et al., 1996; White et al., 1956; Rimstidt and Cole, 1983), and
495 do not form if surfaces are continually bathed in hot-spring water (Jones et al., 1996).
496 Melezhik and Fallick (2001) noted that the silica sinters in the travertines of the KSF may
497 have not been formed in a similar manner to the sinters in modern travertines. Rather, they
498 suggested that the silica was derived from quartz-rich carbonate rocks underlying the
499 travertines, and (hot?) silica-saturated fluids were transported by capillary rise, allowing
500 sinter to be subaerially precipitated by evaporation and cooling.

501 The investigated dolomite cements (type 5; **Fig. 9**) are often composed of feather-shaped
502 dolomite crystals ,Crystals with feather-like shapes are well known in modern travertines
503 (e.g. Fouke et al., 2000; Guo and Riding, 1992; Rainey and Jones, 2009).

Corbella et al. (2004) reported hydrothermal calcite and sulfide stalactites, which outwardly resemble some of the type 3 thinly-laminated crusts and the thicker crusts underlying them. Corbella et al. (2004) described a model of karst and stalactite formation by (i) dissolution of carbonates and (ii) precipitation of sulfides and later carbonates. Their model is based on the mixing of two calcite-supersaturated hydrothermal fluids with different salinities, Ca and bicarbonate ion concentrations and pH levels. They concluded that dissolution and precipitation occur in separate but adjacent zones; dissolution occurs in the zone dominated by brine-rich mixtures and precipitation takes place where low ionic strength groundwaters dominate. A similar model might explain several of the KSF carbonates, whereby brines generated through dissolution of evaporites mixed with low ionic strength groundwaters, causing both cavity formation and carbonate precipitation.

6.2 A comparison to the host carbonates

The background sedimentary dolostones and limestones sampled in Core 5A were studied by Salminen et al. (2013a). Below, their data are compared to the newly obtained isotopic and geochemical results from the cavity fills, crusts and cements.

At the core scale, cavity fills, cements and crusts show in overall similar $\delta^{13}C$ variation (from 4 to 8‰) to that (from 5 to 8 ‰) reported by Salminen et al. (2013a) from the host carbonates (**Fig. 2**). However, the carbonate fills, crusts and cements often show lower $\delta^{13}C$ values compared to the host rocks from comparable depths (**Fig. 2**).

The $\delta^{18}O$ values obtained from cavity fills, crusts and cements show a somewhat different range (from -15 to -8‰) compared to that reported from the host rocks (from -18 to -10‰; Salminen et al., 2013a). This difference could be explained by different depositional

conditions or different fluids. For example, evaporation or a down-flow trend of rising water temperature could explain increasingly higher $\delta^{18}O$ values in the precipitates.

At hand-specimen scale, the cavity fills, crusts and cements show more variation in the $\delta^{13}C$ and $\delta^{18}O$ values than that reported from their host carbonates (Salminen et al., 2013). For example, within a distance of 10 cm, the carbonate fills, crusts and cements show up to 2‰ variation in their $\delta^{13}C$ values and up to 4‰ variation in their $\delta^{18}O$ values.

The investigated carbonate precipitates show coupled $\delta^{13}C$ and the $\delta^{18}O$ trends (**Figs. 11, 14**) In host rocks, only carbonates near contacts with magmatic rocks show statistically significant correlations between the $\delta^{13}C$ and $\delta^{18}O$ values, whereas the bulk carbonates do not, hence suggesting overall good preservation of the C isotope composition (Salminen et al., 2013a).

Coupled $\delta^{13}C$ and the $\delta^{18}O$ trends in carbonate precipitates could indicate metamorphic alteration (Valley, 1986). As the host rocks have generally retained their primary C isotope compositions, it is unlikely that the C isotope composition of the carbonate fills, crusts or cements was significantly affected by metamorphism. A linear correlation between the $\delta^{13}C$ and $\delta^{18}O$ values could instead indicate mixing between two chemically different fluids (Banner et al, 1988; Banner and Hanson, 1990; Lohmann, 1988) or a thermal origin (e.g. Chafetz and Guidry, 2003).

In some cavities, the $\delta^{13}C$ and $\delta^{18}O$ values decrease from the cavity walls towards the cavity center. This could result from the progressively decreasing degree of fluid/bedrock-interaction. Thus higher $\delta^{13}C$ and $\delta^{18}O$ values could indicate more interaction with the host rocks. Alternatively, in some modern speleothem precipitation, kinetic isotope fractionation of C and O results in correlations between the $\delta^{13}C$ and $\delta^{18}O$ values (e.g. Mickler et al.,

2006). However, in the modern speleothems of Mickler et al. (2006), the $\delta^{13}C$ and $\delta^{18}O$ values increase from the rim towards the center – and this is not the case in the KSF.

The surficial dolomite crust at ca. 30.3 m and the possible surficial crust at ca. 27.4 m both show lower $\delta^{13}C$ values and generally lower $\delta^{18}O$ values compared to their host carbonates (**Fig. 2**). In contrast, the similar crust at ca. 68.3 m shows slightly higher $\delta^{13}C$ and $\delta^{18}O$ values than its host carbonates (**Fig. 2**). This latter crust also shows a subtle trend of upwards increasing $\delta^{13}C$ and $\delta^{18}O$ values in its upper half (**Fig. 18**). This pattern might conceivably be related to evaporation (e.g. Stiller et al., 1985). Alternatively, it might be related to temporally (even seasonally?) increasing carbonate precipitation (causing progressive $^{12}CO_2$ loss) upstream of the site of crust deposition, from progressively cooler waters. This is seen in some modern tufa and speleothem systems where mineral precipitation is driven by CO_2 degassing, since subterranean cave ventilation, CO_2 degassing and calcite precipitation, is greater in the winter than the summer (e.g. Matsuoka et al., 2001). However the high pCO_2 of the Paleoproterozoic atmosphere probably argues against such a degassing precipitation mechanism for the KSF precipitates.

.

The investigated cavity fills, crusts and cements often show higher Mn contents than those in their host carbonate rocks, whereas their Sr contents are similar (**Fig. 10**). High Mn contents could imply a thermal origin for the waters, as hot-spring travertines are often characterized by high Mn and Fe contents (e.g. Tanaka et al., 1994; Pentecost, 2005, pp.118). The invesitigated precipitates show upwards decreasing Mn and Fe trends at the core scale (**Fig. 10**), This could indicate decreasing concentrations of soluble iron and manganese in the

carbonate mineral precipitating waters through time, consistent with a temporal change to a more oxidizing environment (e.g. Pentecost, 2005; pp.116; Kah et al., 2012).

In the Upper Dolostone member, the precipitates are slightly less Fe rich than their host rocks (**Fig. 10**). In contrast, the Mn contents are similar to or higher than those in the host rocks (**Fig. 10**). This is perhaps explained by divalent Mn (which can be incorporated into the carbonate mineral lattice) persisting longer in oxidizing travertine-depositing conditions than Fe^{2+} (Pentecost, 2005, pp. 116).

The upwards increasing Sr contents might imply a transition to a more saline environment and opening of a connection to the ocean. This idea is supported by published interpretations of the depositional setting asMelezhik and Fallick (2005) and Salminen et al. (2013b) suggested sea-water invasion during the deposition of the upper part of the KSF. Higher Sr contents could also imply dissolution of the calcitic host rocks in the uppermost part of the succession. Calcite in general contains less Mn and more Sr than dolomite (e.g. Gaucher et al., 2007).

Samples distribute into four groups according to the co-variation plots (**Fig. 11**). (I) Majority of the samples is plotted in the group, which is characterized by relatively high $\delta^{13}C$ values (ca. 6–8 ‰), moderate to low $\delta^{18}O$ values (ca. -10 to -15‰), relatively low Mn contents (up to 1000 ppm) and Sr contents (<200 ppm). (II) Another group includes some cavity and vein fills (chiefly dolospar representing the **latest infill**) with **high $\delta^{18}O$ values** (ca. -9 to -8 ‰), high $\delta^{13}C$ values (ca. 7-8 ‰), and low Mn (<500 ppm) and Sr contents (≤120 ppm). (III) Second minor group includes different types of samples with **low** $\delta^{13}C$ values (<6 ‰), low $\delta^{18}O$ values (≤11 ‰), high Mn contents (> 1000 ppm) and low to moderate Sr contents. (IV) One more minor group consist of a few samples (cavity and vein precipitates and one

subsample from a surficial crust) from the Upper Dolostone member with high $\delta^{13}C$ values, moderate $\delta^{18}O$ values, **high Sr contents** and low Mn contents.

Samples in the group I likely show also geochemical characteristics of the dissoluted dolomitic host rocks, whereas the group IV probably indicates dissolution of calcitic (and dolomitic) host rocks. Group III samples perhaps represent "pure" deep-sourced fluid, as implied by the low $\delta^{13}C$ values and high Mn contents. Group II represents the last dolomite generation/phase.

6.3 Comparison to previous investigations of the KSF travertines

Some carbonates investigated in Core 5A (e.g. the cavity at ca. 81.4 m) resemble the travertines studied by Melezhik and Fallick (2001) and Melezhik et al., (2004) from other locations in the KSF. Melezhik and Fallick (2001) reported $\delta^{13}C$ values from 0.8 to 7.2‰ and $\delta^{18}O$ values from -12.4 to -9.8‰ in a travertine crust. They also reported a much greater range of $\delta^{13}C$ and $\delta^{18}O$ ratios (from -6.1 to 7.7‰ and from -18.3 to -9.1‰, respectively) in a travertine mound. Even the lowest $\delta^{13}C$ values found in the current study are several per-mils higher than the lowest $\delta^{13}C$ values reported by Melezhik and Fallick (2001). They explained the observed $\delta^{13}C$ and $\delta^{18}O$ variations and trends by invoking initial CO_2 out-gassing at the hot-spring orifice, down-flow trends of thermal waters (following modern examples e.g. Friedman, 1970; Chafetz et al., 1991; Chafetz and Lawrence, 1994), mixing with ambient

waters, and possible evaporation. The travertine crusts were suggested to be precipitated in shallow distal pools, periodically fed by the thermal springs (Melezhik and Fallick, 2001).

Upwards (within cavities/crusts) increasing or decreasing $\delta^{13}C$ and $\delta^{18}O$ trends and cyclical variations of $\delta^{13}C$ and $\delta^{18}O$ values were found in the investigated precipitates from Core 5A. Such fluctuations could be explained by the model of Melezhik and Fallick (2001). The upward $\delta^{13}C$ increase would then be explained by a down-flow trend, possibly connected to evaporation and some mixing with ambient water in the depositional basin. The upwards decreasing $\delta^{13}C$ and $\delta^{18}O$ trends could be explained by a resurgence in supply of hot-spring water to the point of travertine precipitation (such as a distal pool). The cyclical $\delta^{13}C$ pattern in the crust at ca. 30.3 m could indicate pulsed supply of the thermal waters, connected to intervals of intense evaporation.

Melezhik and Fallick (2001) and Melezhik et al. (2004) found that travertines and the stratified dolostone of the KSF plot along two entirely different lines in a $\delta^{13}C$-$\delta^{18}O$ cross-plot. Melezhik et al. (2004) found that travertines show positive correlation between the $\delta^{13}C$ and $\delta^{18}O$ values, whereas no significant correlation between them is found in the stratified dolostone . Like the travertines investigated by Melezhik et al. (2004), the cavity fills, crusts and cements in Core 5A show positive co-variation between the $\delta^{13}C$ and $\delta^{18}O$ values (**Fig. 14**), while only the contact-altered host carbonate show co-variation between $\delta^{13}C$ and $\delta^{18}O$ values (Salminen et al., 2013a). Thus, the investigated carbonate precipitates of Core 5A also plot differently on a $\delta^{13}C$-$\delta^{18}O$ cross-plot to their host rocks.

Melezhik and Fallick (2003) reported variable $\delta^{13}C$ and $\delta^{18}O$ values from dolospar/dolomicrospar cements and fills in fenestrae and voids. They did not find significant differences between the $\delta^{13}C$ values of such cements and fills and their host dolomicrite . They did find that the $\delta^{18}O$ values in the dolospar/dolomicrospar were somewhat lower to

643 those in the host dolomicrite, hence were explained by syn-depositional/early diagenetic
644 alteration processes. In Core 5A, the $\delta^{13}C$ values are commonly lower in the cavity fills,
645 crusts and cements than in their host carbonate rocks, suggesting that an external lower $\delta^{13}C$
646 carbon source is required. It is plausible that all the investigated carbonate precipitates from
647 Core 5A could have been precipitated from ^{13}C-depleted fluids.

648

649 **6.4 The origin of the cavity fills, crusts and cements in the KSF**

650

651 An external carbon source would explain the lower $\delta^{13}C$ values in the cavity fills, crusts and
652 cements compared to the surrounding host rock. That source could be (i) CO_2-bearing
653 meteoric water, (ii) CO_2 derived from oxidation of organic carbon, or (iii) deep-sourced CO_2.
654 As the sedimentary rocks in the KSF are devoid of organic carbon (e.g. Melezhik and Fallick,
655 2005), it seems unlikely that the external carbon comes directly from an organic source.
656 Ameteoric water with low $\delta^{13}C$ dissolved inorganic carbon is a possibility, though this would
657 have implications for the record of life in Paleoproterozoic terrestrial environments. The
658 external carbon could also be derived from deep-sourced CO_2, as magmatic carbon
659 commonly has $\delta^{13}C$ values around -5 to -7‰ (e.g. Anderson and Arthur, 1983; Deines, 2002).

660 Several possible mechanisms could be invoked to explain how these carbonate rocks formed
661 under a high pCO_2 atmosphere and without high pCO_2 soils (Brasier, 2011).

662 Paleoproterozoic speleothem may have been formed **(1) under an ice cover due to warming**
663 **of waters** (Dreybrodt, 1982), and alternatively **(2) freezing of water** could have caused
664 carbonate precipitation in caves (e.g. Aharon, 1988). However, no petrographic or structural
665 evidence for glaciation is present in the KSF and these two models cannot explain the
666 observed $\delta^{13}C$ and $\delta^{18}O$ trends.

667 Precipitation may have been aided by **(3) cyanobacteria and microbes** (e.g. Merz, 1992;
668 Spiro and Pentecost, 1991). As stromatolites are found in the KSF, it is possible that
669 cyanobacteria influenced precipitation of crusts. However the formation of the cavity fills and
670 veins cannot be explained by photosynthetic cyanobacteria.

671 Carbonates are today usually dissolved by fluids rich in carbonic acid (H_2CO_3). However,
672 fluids rich in other acids may also cause carbonate dissolution. For example, **(4) sulfuric acid**
673 (H_2SO_4) has been reported to cause dissolution (e.g. Atkinson, 1983). Local H_2SO_4
674 production in the Paleoproterozoic was likely increased due to the oxygenation of the
675 atmosphere and the oxidation of sulfides (Bekker and Holland, 2012; Brasier, 2011). But
676 sulfuric acid dissolution alone could not itself explain the precipitation of the cavity fills.

677 Karst and speleothem-like precipitates can also be formed by local **(5) calcite**
678 **supersaturation due to** a **common-ion effect**: extra calcium is supplied e.g. from dissolution
679 of evaporites (e.g. Calaforra et al., 2008; Wigley, 1973a) or incongruent dissolution of
680 dolomite (e.g. Wigley, 1973b). This leads to calcite precipitation when the solution becomes
681 supersaturated with respect to calcite. The common-ion effect is found in polymineralic
682 systems (calcite and gypsum, or calcite and dolomite) that are initially calcite saturated (*see*
683 *Brasier, 2011*). Such a common-ion effect causes precipitation in some modern hot springs
684 (Pentecost, 1995) and in cold (~6.5°C) springs (Omelon et al., 2006) in the presence of
685 gypsum. It can also explain the precipitation of lake tufas (Dunn, 1953). Thus, the common-
686 ion effect could also explain the formation of the surficial crusts and cements in the KSF.

687 The **common-ion effect caused by dissolution of evaporites (5a)** may explain the formation
688 of the small-scale cavities and the precipitation of the carbonate fills and the surficial
689 precipitates in the KSF. Probable sulfate pseudomorphs have previously been reported from
690 the KSF (e.g. Melezhik and Fallick, 2005), and they were also found in this study. The

691 common-ion effect due to dissolution of Ca-evaporites (e.g. gypsum) results in precipitation
692 of calcite (e.g. Wigley, 1973a). Calcite, however, is only a minor constituent in the cavities of
693 the KSF, and there is no clear evidence of calcite recrystallizing to dolomite. Dolomites could
694 have been precipitated due to a common-ion effect caused by dissolution of Mg-rich
695 evaporites. However, pseudomorphs after Mg-rich evaporites have not been found in the
696 KSF.

697 The **common-ion effect caused by dissolution of dolomite (5b)** is a possible explanation, as
698 the host carbonates in the formation are mainly dolostones. However, Wigley (1973b) noted
699 that the incongruent dissolution of dolomite leads to the precipitation of calcite prior to
700 dolomite. Incongruent dissolution of dolomite is an unlikely explanation for the formation of
701 the precipitates. Thus, the common-ion effect could explain the karst solution in the KSF, but
702 does not obviously explain the precipitation of chiefly dolomitic precipitates.

703 Degassing can also happen due to **(6) boiling** (in addition to high temperature) in springs
704 (e.g. Arnósson, 1989). Temperatures well below the boiling point cause travertine
705 precipitation today (e.g. Fouke et al., 2000), but meteoric waters can also be heated when
706 percolating through the bedrock (e.g. Dublyansky, 1995; Djidi et al., 2008). Boiling meteoric
707 waters could cause carbonate precipitation, but might not explain all the observed $\delta^{13}C$ and
708 $\delta^{18}O$ trends. Moreover, heating of meteoric waters could be connected to supply of deep-
709 sourced CO_2 (Djidi et al., 2008).

710 **Deep-sourced CO_2 (7)** could explain the formation of the cavity fills, surficial dolomite
711 crusts and dolomite cements in the KSF (e.g. Duliński et al., 1995; Pentecost and Viles, 1994;
712 Yoshimura et al., 2004). Deep-sourced CO_2 could be either volcanic or produced by
713 metamorphic reactions, and is usually associated with hydrothermal activity (e.g. Pentecost
714 and Viles, 1994; Pentecost, 1995). Deep-sourced CO_2 can increase the dissolution rates as

715 well as carbonate precipitation even in ambient water temperatures (Yoshimura et al., 2004),
716 but some of the investigated precipitates have physical and geochemical characteristics (e.g.
717 veins that could have been fluid conduits; mound morphologies; feather-shaped crystals, high
718 Mn contents, co-variation and trends of $\delta^{13}C$ and $\delta^{18}O$) that are at least consistent with deep-
719 sourced fluids and hot-spring travertine.

720 The isotope results from Core 5A samples do not show unambiguous evidence of a deep-
721 sourced origin or deposition in close vicinity to hot-spring vents. However, the carbonate
722 precipitates in the KSF could have precipitated from thermal waters distally from the vents,
723 as suggested by Melezhik and Fallick (2001).

724 The most likely explanation for the formation of the carbonate precipitates in the KSF is
725 apparently deep-sourced CO_2, connected to hydrothermal activity. Boiling may have
726 contributed to the carbonate precipitation and deep-sourced fluids may have mixed with
727 meteoric waters. Thus, the cavity and vein fills in the KSF could represent hydrothermal karst
728 ("cave travertine"). Dolomite cements and some of the surficial crusts are likely travertine,
729 although some dolomite crusts could represent evaporite layers. The Mn/Sr ratios, elemental
730 contents and their patterns in the vein at 53.7 m in Core 5A could suggest formation during
731 burial.

732 If pseudomorphs or relicts of Mg-rich evaporites were later found in the KSF, the common-
733 ion effect connected to dissolution of evaporites could also explain the formation of the
734 cavities and the cavity fills, crusts and cements.

735

736 **6.5 The depositional setting of the KSF**

737

738 Salminen et al. (2013b) interpreted the depositional setting of Core 5A as deltaic and
739 lacustrine, but tidally influenced. Melezhik and Fallick (2005) concluded that the depositional
740 setting of the KSF was deltaic and shallow lacustrine. This new investigation supports the
741 previous interpretations of the depositional setting of the KSF.

742 Melezhik and Fallick (2001) pointed out that the modern travertines are only found in
743 terrestrial settings. Most of the investigated cavity fills, crusts and cements are likely
744 travertine or "cave travertine". We infer they precipitated in terrestrial settings.

745 Melezhik et al. (2004) investigated various subaerial exposure surfaces in the KSF. Findings
746 of this study also support occasional subaerial exposure during the deposition of the KSF.
747 The red color in the dolomite crusts likely indicates oxic conditions, possibly in a subaerial
748 environment.. Likely evaporitic sulfate pseudomorphs were also found.

749 The question of how the deep-sourced CO_2 was supplied to the carbonate sediments in the
750 KSF is open. One possibility is through the veins (now cemented up); another is through syn-
751 depositional faulting, as the KSF was likely deposited in an intracontinental rift setting
752 (Melezhik and Sturt, 1994). Melezhik and Fallick (2005) provided a reconstruction of the
753 Kuetsjärvi rift-related lake, which includes hydrothermal springs and transverse faults.
754 Eruption of later volcanic rocks of the Kuetsjärvi Volcanic Formation may also have
755 provided a source for the formation of cavity and vein fills, which are apparently secondary
756 precipitates. However, this cannot explain the deposition of the surficial precipitates.

757

758 ## 7. Conclusions

759

760 Core 5A was obtained from the Paleoproterozoic Kuetsjärvi Sedimentary Formation. Drilled
761 stratified carbonate rocks contain dolomite crusts, dolomite cements and abundant small-
762 scale cavities and veins. These cavities and veins are mainly filled with dolomite and quartz.
763 Dolomite crusts occur in the cavities and on bedding/erosional surfaces. Dolomite cements
764 are found on uneven surfaces encrusting sandstone fragments. Dolomite crusts, cements and
765 carbonate fills were analyzed for $\delta^{13}C$ and $\delta^{18}O$ values and selected acid-soluble elements.
766 The newly obtained results were compared to the published results from the host carbonates.

767 The investigated carbonate precipitates show lower or similar $\delta^{13}C$ values to their host
768 carbonates. The lower $\delta^{13}C$ values suggest the presence of an external carbon source, which
769 was likely deep-sourced/hydrothermal CO_2. Dolomite cements and the dolomite crusts on
770 bedding/erosional surfaces are likely thermal travertines. This is supported by the
771 petrographic and geochemical observations. In the absence of organic carbon rich soils, deep-
772 sourced/hydrothermal CO_2 also provides a very plausible explanation for the formation of the
773 cavities, veins and carbonate fills. Cavity fills may be interpreted as “cave travertine”. Some
774 veins may represent burial veins, or could have been conduits through which the travertine-
775 precipitating fluids passed.

776 The $\delta^{13}C$ and $\delta^{18}O$ values show positive correlation. Both upwards increasing and decreasing
777 $\delta^{13}C$ and $\delta^{18}O$ trends were found in the dolomite crusts. These trends could be explained by
778 down-flowing thermal water possibly affected by evaporation and/or modified due to mixing
779 with the ambient waters. Dolomite crusts showing only upwards increasing $\delta^{13}C$ trends could
780 represent dolomitized evaporite layers. The $\delta^{13}C$ and $\delta^{18}O$ values commonly show increasing
781 trends from the middle of the cavity towards the cavity walls, probably indicating different
782 degrees of mixing with the host rocks and thermal waters.

Few reports have been published on Precambrian travertine or speleothem. The above new detailed geochemical data and petrographic analyses ofwhat may be Earth´s earliest travertines provide a glimpse of complexity in textures and facies likely quite similar to that found in modern hot-spring settings. Consideration of several possible depositional mechanisms leads to the conclusion that these are two billion year old hot-spring travertines likely formed by similar processes to those of the modern world.

Acknowledgements

PES was supported by Väisälä Foundation (Finnish Academy of Science and Letters) and the Finnish Doctoral Program in Geology. This is a contribution (paper) to the ICDP FAR-DEEP project.

References

Aharon, P., 1988. Oxygen, carbon and U-series isotopes of aragonites from Vestfold Hills, Antarctica: clues to geochemical processes in subglacial environments. Geochimica et Cosmochimica Acta 52, 2321-2331.

Amelin, Yu.V., Heaman, L.M., Semenov, V.S., 1995. U–Pb geochronology of layered mafic intrusions in the eastern Baltic Shield: implications for the timing and duration of Paleoproterozoic continental rifting. Precambrian Research 75, 31-46.

Anderson, T.F., Arthur, M.A., 1983. Stable isotopes of oxygen and carbon and their application to sedimentologic and paleoenvironmental problems, in: Arthur, M.A., Anderson, T.F., Kaplan, I.R., Veizer, J., Land, L.S. (Eds.), Stable Isotopes in Sedimentary Geology, Volume 10, Columbia SC: SEPM Short Course.

807 Andrews, J.E., Brasier, A.T., 2005. Seasonal records of climatic change in annually laminated tufas: short
808 review and future prospects. Journal of Quaternary Science 20, 411-421.
809
810 Arnórsson, S., 1989. Deposition of calcium carbonate minerals from geothermal waters — theoretical
811 considerations. Geothermics 18, 33-39.
812 Atkinson, T.C., 1983. Growth mechanisms of speleothems in Castleguard Cave, Columbia Icefields, Alberta,
813 Canada. Arctic and Alpine Research 15, 523-536.
814 Awramik, S.M., Buchheim, H.P., 2009. A giant, Late Archean lake system: the Meentheena member (Tumbiana
815 Formation: Fortescue Group), Western Australia. Precambrian Research 174, 215-240.
816
817
818
819 Baker, A.J., Fallick, A.E., 1989a. Evidence from Lewisian limestones for isotopically heavy carbon in two-
820 thousand-million-year-old sea water. Nature 337, 352-354.
821 Baker, A.J., Fallick, A.E., 1989b. Heavy carbon in two-billion-year-old marbles from Lofoten-Vesterålen,
822 Norway: implications for the Precambrian carbon cycle. Geochimica et Cosmochimica Acta 53, 1111-
823 1115.
824 Banner, J.L., Hanson, G.N., 1990. Calculation of simultaneous isotopic and trace element variations during
825 water–rock interaction with applications to carbonate diagenesis. Geochimica et Cosmochimica Acta, 54,
826 3123-3137.
827 Banner, J.L., Hanson, G.N. and Meyers, W.J., 1988. Water–rock interaction history of regionally extensive
828 dolomites of the Burlington-Keokuk Formation (Mississippian): isotopic evidence, in: Shukla, V., Baker,
829 P.A. (Eds.), Sedimentology and Geochemistry of Dolostones. SEPM Special Publication 43, 97-113.
830 Bekker A., Kaufman, A.J., Karhu, J.A., Beukes, N.J., Swart, Q.D., Coetzee, L.L., Eriksson, K.E., 2001.
831 Chemostratigraphy of the Paleoproterozoic Duitschland Formation, South Africa: Implications for
832 coupled climate change and carbon cycling. American Journal of Science 301, 261-285.
833 Bekker, A., Holland, H.D., 2012. Oxygen overshoot and recovery during the early Paleoproterozoic. Earth and
834 Planetary Science Letters 317-318, 295-304.
835 Berthelsen, A., Marker, M., 1986. Tectonics of the Kola collision suture and adjacent Archaean and Early
836 Proterozoic terrains in the northeastern region of the Baltic Shield. Tectonophysics 126, 31-55.

837 Brasier, A.T., 2011. Searching for travertines, calcretes and speleothems in deep time: Processes, appearances,
838 predictions and the impact of plants. Earth-Science Reviews 104, 213-239.
839 Brasier, A.E., Salminen, P.E., Melezhik, V.A., Fallick, A.E., 2013. Earth´s Earliest Travertines, in: Melezhik,
840 V.A., Kump, L.R., Fallick, A.E., Strauss, H., Hanski, E.J., Prave, A.R., Lepland, A. (Eds.): Reading the
841 Archive of Earth´s Oxygenation. Volume 3: Global Events and the Fennoscandian Arctic Russia –
842 Drilling Early Earth Project. Springer-Verlag, Berling Heidelberg, Chapter 7.9.4, pp. 1435-1456.
843 Calaforra, J., Forti, P., Fernandez-Cortes, A., 2008. Speleothems in gypsum caves and their paleoclimatological
844 significance. Environmental Geology 53, 1099-1105.
845 Chafetz, H.S., Guidry, S.A., 2003. Deposition and diagenesis of Mammoth Hot Spring travertine, Yellowstone
846 National Park, Wyoming, USA. Canadian Journal of Earth Sciences 40, 1515-1529.
847 Chafetz, H.S., Lawrence, J.R., 1994. Stable isotopic variability within modern travertines. Géographie physique
848 et Quaternaire 48, 257-273.
849 Chafetz, H.S., Rush, P.F., Utech, N.M., 1991. Microenvironmental controls on mineralogy and habit of $CaCO_3$
850 precipitates: an example from an active travertine system. Sedimentology 38, 107-126.
851 Corbella, M., Ayora, C., Cardellach, E., 2004. Hydrothermal mixing, carbonate dissolution and sulfide
852 precipitation in Mississippi Valley-type deposits. Mineralium Deposita 39, 344-357.
853 Deines, P. 2002. The carbon isotope geochemistry of mantle xenoliths. Earth Science Reviews 58, 247-278.
854 Djidi K., Bakalowicz, M., Benali, A.M., 2008. Mixed, classical and hydrothermal karstification in a carbonate
855 aquifer: Hydrogeological consequences. The case of the Saida aquifer system, Algeria. Comptes Rendus
856 Geoscience 340, 462-473.
857 Dreybrodt, W., 1982. A possible mechanism for growth of calcite speleothems without participation of biogenic
858 carbon dioxide. Earth and Planetary Science Letters 58, 293-299.
859 Dublyansky, Y.V. 1995. Speleogenetic history of the Hungarian hydrothermal karst. Environmental Geology
860 25, 24-35.
861 Duliński, M., Grabczak, J., Kostecka, A., Weclawik, S., 1995. Stable isotope composition of spelean calcites
862 and gaseous CO_2 from Tylicz (Polish Carpathians). Chemical Geology 125, 271-280.
863 Dunn, J.R., 1953. The origin of the deposits of tufa in Mono Lake. Journal of Sedimentary Research 23, 18-23.
864 Fairchild, I.J., Borsato, A., Tooth, A.F., Frisia, S., Hawkesworth, C.J., Huang, Y., McDermott, F., Spiro, B.,
865 2000. Controls on trace element (Sr-Mg) compositions of carbonate cave waters: implications for
866 speleothem climatic records. Chemical Geology 166, 255-269.

867 Ford, T.F., Pedley, H.M., 1996. A review of tufa and travertine deposits of the world. Earth-Science Reviews
868 41, 117-175.
869 Fouke, B.W., Farmer, J.D., Des Marais, D.J., Pratt L., Sturchio, N.C., Burns, P.C., Discipulo, M.K., 2000.
870 Depositinal facies and aqueous-solid geochemistry of travertine-depositing hot springs (Angel Terrace,
871 Mammoth Hot Springs, Yellowstone National Park, USA). Journal of Sedimentary Research 70, 565-
872 585.
873 Friedman, I., 1970. Some investigations of deposition of travertine from Hot Springs: Part I. The isotopic
874 chemistry of a travertine-depositing spring. Geochimica et Cosmochimica Acta 34, 1303-1315.
875 Frisia, S., Borsato, A., 2010. Karst, in: Alonso-Zarza, A.M. and Tanner, L.H., Carbonates in Continental
876 Settings: Facies, Environments and Processes. Developments in Sedimentology v. 61, p. 269-318.
877 Elsevier, Amsterdam.
878 Gaucher, C., Sial, A.N., Ferreira, V.P., Pimentel, M.M., Chiglino, L., Sprechmann, P., 2007. Chemostratigraphy
879 of the Cerro Victoria Formation (Lower Cambrian, Uruguay): evidence for progressive climate
880 stabilization across the Precambrian–Cambrian boundary. Chemical Geology 237, 28-46.
881 Gómez Peral, L.E., Poiré, D.G., Strauss, H., Zimmermann, U., 2007. Chemostratigraphy and diagenetic
882 constraints on Neoproterozoic carbonate successions from the Sierras Bayas Group, Tandilia System,
883 Argentina. Chemical Geology 237, 109-128
884 Guo, L., Riding, R., 1992. Aragonite laminae in hot water travertine crusts, Rapolano Terme, Italy.
885 Sedimentology 39, 1067-1079.
886 Gutzmer, J., Beukes, N.J., 1998. Earliest laterites and possible evidence for terrestrial vegetation in the Early
887 Proterozoic. Geology 26, 263-266.
888 Hoffman, P., 1975. Shoaling-upward shale-to-dolomite cycles in the Rocknest Formation (Lower Proterozoic),
889 Northwest Territories, Canada, in: Ginsburg, R.N. (Ed.), Tidal Deposits: a casebook of recent examples
890 and fossil counterparts. Springer/Verlag, New York, pp.257-265.
891 Hoffman, P.,1976. Environmental diversity of Middle Precambrian stromatolites, in: Walter, M. (Ed.),
892 Stromatolites, Developments in sedimentology. Elsevier, Amsterdam, pp. 599-611.
893 James, N.P., Narbonne, G.M., Kyser, T.K., 2001. Late Neoproterozoic cap carbonates: Mackenzie Mountains,
894 northwestern Canada: precipitation and global glacial meltdown. Canadian Journal of Earth Sciences 38,
895 1220-1262.

Jiang, G., Christie-Blick, N., Kaufman, A.J., Banerjee, D.M., Rai, V., 2003. Carbonate platform growth and cyclicity at a terminal Proterozoic passive margin, Infra Krol Formation and Krol Group, Lesser Himalaya, India. Sedimentology 50, 921-952

Jones, B., Renaut, R.W., 2008. Cyclic development of large, complex, calcite dendrite crystals in the Clinton travertine, Interior British Columbia, Canada. Sedimentary Geology 203, 17-35.

Jones, B., Renaut, R.W., Rosen, M., 1996. High-temperature (>90°C) calcite precipitation at Waikite Hot Spring, North Island, New Zealand. Journal of the Geological Society 153, 481-496.

Kah, L.C., Bartley, J.K., Teal, D.A., 2012. Chemostratigraphy of the Late Mesoproterozoic Atar Group, Taoudeni Basin, Mauritania: Muted isotopic variability, facies correlation, and global isotopic trends. Precambrian Research 200-203, 82-103.

Karhu, J.A., 1993. Paleoproterozoic evolution of the carbon isotope ratios of sedimentary carbonates in the Fennoscandian Shield. Geological Survey of Finland Bulletin 371, 1-87.

Karhu, J.A., Holland, H.D., 1996. Carbon isotopes and the rise of atmospheric oxygen. Geology 24, 867-870.

Karhu, J.A., Melezhik, V.A., 1992. Carbon isotope systematics of early Proterozoic sedimentary carbonates in the Kola Peninsula, Russia: correlations with Jatulian formations in Karelia, in: Balagansky, V.V., Mitrofanov, F.P. (Eds.), Correlation of Precambrian Formation of the Kola-Karelia Region and Finland. Kola Scientific Centre of the Russian Academy of Sciences, Apatity, pp. 48-53.

Kaufman, A.J., Knoll, A.H., 1995. Neoproterozoic variations in the C-isotopic composition of seawater: stratigraphic and biogeochemical implications. Precambrian Research 73, 27-49.

Lohmann, K.C., 1988. Geochemical patterns of meteoric diagenesis systems and their application to studies of paleokarst, in: James, N.P., Choquette, P.W. (Edit), Paleokarst. Springer-Verlag, New York, pp.58-80.

Martin, A.P., Condon, D.J., Prave, A.R., Melezhik, V.A., Lepland, A., Fallick, A.E., 2013. Dating the termination of the Palaeoproterozoic Lomagundi-Jatuli carbon isotopic event in the North Transfennoscandian Greenstone Belt. Precambrian Research 224, 160-168.

Matsuoka, J., Kano, A., Oba, T., Watanabe, T., Sakai, S., Seto, K., 2001. Seasonal variation of stable isotopic compositions recorded in a laminated tufa, SW Japan. Earth and Planetary Science Letters 192, 31-44.

Melezhik, V.A., 1992. Palaeoproterozoic Sedimentary and Rock-Forming Basins of the Fennoscandian Shield. Nauka (Science), Leningrad, 258 p. (in Russian.)

Melezhik, V.A., Fallick, A.E., 2001. Palaeoproterozoic travertines of volcanic affiliation from a ^{13}C-rich rift lake environment. Chemical Geology 173, 293-312.

926 Melezhik, V.A., Fallick, A.E., 2003. $\delta^{13}C$ and $\delta^{18}O$ variations in primary and secondary carbonates: several
927 contrasting examples from Palaeoproterozoic ^{13}C-rich metamorphosed dolostones. Chemical Geology
928 201, 213-228.
929 Melezhik, V.A., Fallick, A.E., 2005. Palaeoproterozoic, rift-related, ^{13}C-rich, lacustrine carbonates, NW Russia.
930 Part I: Sedimentology and major element geochemistry. Transactions of the Royal Society of Edinburgh:
931 Earth Sciences 95, 393-421.
932 Melezhik, V.A., Fallick, A.E., Grillo, S.M., 2004. Subaerial exposure surfaces in a Palaeoproteroizoic ^{13}C-rich
933 dolostone sequence from the Pechenga Greenstone Belt: palaeoenvironmental and isotopic implications
934 for the 2330-2060 Ma global isotope excursion of $^{13}C/^{12}C$. Precambrian Research 133, 75-103.
935 Melezhik, V.A., Fallick, A.E., Kuznetsov, A.B., 2005. Palaeoproterozoic, rift-related, ^{13}C-rich, lacustrine
936 carbonates, NW Russia. Part II: Global isotope signal recorded in the lacustrine dolostones. Transactions
937 of the Royal Society of Edinburgh: Earth Sciences 95, 423-444.
938 Melezhik, V.A., Huhma, H., Condon, D.J., Fallick, A.E., Whitehouse, M.J., 2007. Temporal constraints on the
939 Paleoproterozoic Lomagundi-Jatuli carbon isotopic event. Geology 35, 655-658.
940 Melezhik, V.A., Sturt, B.A., 1994. General geology and evolutionary history of the early Proterozoic Polmak-
941 Pasvik-Pechenga-Imandra/Varzuga-Ust'Ponoy Greenstone Belt in the north-eastern Baltic Shield. Earth-
942 Science Reviews 36, 205-241.
943 Merz, M.U.E., 1992. The Biology of Carbonate Precipitation by Cyanobacteria. Facies 26, 81-102.
944 Mickler, P.J., Stern, L.A., Banner, J.L., 2006. Large kinetic isotope effects in modern speleothem. Geological
945 Society of America Bulletin 118, 65-81.
946 Omelon, C.R., Pollard, W.H., Andersen, D.T., 2006. A geochemical evaluation of perennial spring activity and
947 associated mineral precipitates at Expedition Fjord, Axel Heiberg Island, Canadian High Arctic. Applied
948 Geochemistry 21, 1-15.
949 Pedley, H.M., 1990. Classification and environmental models of cool freshwater tufas. Sedimentary Geology
950 68, 143-154.
951 Pelechaty, S.M., James, N.P., Kerans, C., Grotzinger, J.P., 1991. A middle Proterozoic palaeokarst
952 unconformity and associated sedimentary rocks, Elu Basin, northwest Canada. Sedimentology 38, 775-
953 797.
954 Pentecost, A., 1993. British travertines: A review. Proceedings of the Geologists Association 104, 23-39.

955 Pentecost, A., 1995. Geochemistry of carbon dioxide in six travertine-depositing waters of Italy. Journal of
956 Hydrology 167, 263-278.
957 Pentecost, A., 2005. Travertine. Springer–Verlag, Berlin. 446 pp.
958 Pentecost, A., Viles, H., 1994. A review and reassessment of travertine classification. Géographie Physique et
959 Quaternaire 48, 305-314.
960 Petrov, V.P., Voloshina, I.M., 1995. Regional metamorphism of the Pechenga area rocks, in: Mitrofanov, F.P
961 and Smol´kin, V.F. (Eds), Magmatism, Sedimentogenesis and Geodynamics of the Pechenga Paleorift.
962 Apatity. Kola Science Centre, p. 164–82. (in Russian).
963 Praekelt, H.E., Germs, G.J.B., Kennedy, J.H., 2008. A distinct unconformity in the Cango Caves Group of the
964 Neoproterozoic to early Paleozoic Saldania Belt in South Africa: its regional significance. South African
965 Journal of Geology 111, 357-368.
966 Predovsky, A.A., Fedotov, Zh.A., Ahkmedov, A.M., 1974. Geochemistry of the Pechenga Complex. Nauka
967 (Science), Leningrad, 139 p. (in Russian).
968 Rainbird, R.H., Davis, W.J., Stern, R.A., Peterson, T.D., Smith, S.R., Parrish, R.R., Hadlari, T., 2006. Ar–Ar
969 and U–Pb Geochronology of a Late Paleoproterozoic Rift Basin: Support for a Genetic Link with
970 Hudsonian Orogenesis, Western Churchill Province, Nunavut, Canada. Journal of Geology 114, 1-17.
971 Rainey, D.K., Jones, B., 2009. Abiotic versus biotic controls on the development of the Fairmont Hot Springs
972 carbonate deposit, British Columbia, Canada. Sedimentology 56, 1832-1857.
973 Renaut, R.W., Jones, B., 1997. Controls on aragonite and calcite precipitation in hot springs travertines at
974 Chemurkeu, Lake Bogoria, Kenya. Canadian Journal of Earth Sciences 34, 801-818.
975 Riding, R., 1991. Classification of microbial carbonates, in: Riding, R. (Ed.), Calcareous algae and
976 stromatolites. Springer, Berlin, p. 21-51.
977 Riding, R., 2000. Microbial carbonates: the geological record of calcified bacterial-algal mats and biofilms.
978 Sedimentology 47, 179-214.
979 Rimstidt, J.D., Cole, R.R., 1983. Geothermal mineralization I: the mechanism of formation of the Beowawe,
980 Nevada, siliceous sinter deposit. American Journal of Science 283, 861-875.
981 Rogerson, M., Pedley, H.M., Kelham, A. 2014. Linking mineralization process and sedimentary product in
982 terrestrial carbonates using a solution thermodynamic approach. Earth Surface Dynamics 2, 197-216.
983 Salminen, P.E., Karhu, J.A., Melezhik, V.A., 2013a. Tracking lateral $\delta^{13}C_{carb}$ variation in the Paleoproterozoic
984 Pechenga Greenstone Belt, the north eastern Fennoscandian Shield. Precambrian Research 228, 177-193.

985 Salminen, P.E., Melezhik, V.A., Hanski, E.J., Lepland, A., Romashkin, A.E., Rychanchik, D.V., Luo, Zh.-Y.,
986 Sharkov, E.V., Bogina, M.M., 2013b, Kuetsjärvi Sedimentary Formation: FAR-DEEP Hole 5A,
987 neighbouring quarry and related outcrops, in: Melezhik, V.A., Prave, A.R., Fallick, A.E., Hanski E.J.,
988 Lepland, A., Kump, L.R., Strauss, H. (Eds.). Reading the Archive of Earth's Oxygenation. Volume 2:
989 The Core Archive of the Fennoscandian Arctic Russia-Drilling Early Earth Project. Springer-Verlag,
990 Berlin Heidelberg, Chapter 6.2.2, p. 617-649.
991
992 Shields, G.A., Brasier, M.D., Stille, P., Dorjnamjaa, D.-i., 2002. Factors contributing to high $\delta^{13}C$ values in
993 Cryogenian limestones of western Mongolia. Earth and Planetary Science Letters 196, 99-111.
994 Shields, G.A., Deynoux, M., Strauss, H., Paquet, H., Nahon, D., 2007. Barite-bearing cap dolostones of the
995 Taoudéni Basin, northwest Africa: Sedimentary and isotopic evidence for methane seepage after a
996 Neoproterozoic glaciation. Precambrian Research 153, 209-235.
997 Skotnicki, S.J., Knauth, L.P., 2007. The Middle Proterozoic Mescal Paleokarst, Central Arizona, U.S.A.: karst
998 development, silicification, and cave deposits. Journal of Sedimentary Research 77, 1046-1062.
999 Spiro, B., Pentecost, A., 1991. One day in the life of a stream: a diurnal inorganic carbon mass balance for a
1000 travertine-depositing stream (waterfall beck, Yorkshire). Geomicrobiology Journal 9, 1-11
1001 Stiller, M., Rounick, J.S., Shasha, S., 1985. Extreme carbon-isotope enrichments in evaporitic brines. Nature
1002 316, 434-435.
1003 Tanaka, A., Seyama, H., Soma, M. 1994. Iron- and manganese-rich sediments as an indicator of hot spring
1004 activities at the bottom of Lake Mashu, Japan. Geochemical Journal 28, 289-306.
1005 Valley, J.W., 1986. Stable isotope geochemistry of metamorphic rocks, in: Valley, J.W., Taylor, H.P., O'Neil,
1006 J.R. (Eds.), Stable Isotopes in High Temperature Geological Processes. Reviews in Mineralogy, Volume
1007 16, Mineralogical Society of America, Washington, pp. 445-489.
1008 Veizer, J., 1983. Chemical diagenesis of carbonates: theory and application of the trace element technique, in:
1009 Arthur, M.A., Anderson, T.F., Kaplan, I.R., Veizer, J., Land, L.S. (Eds.), Stable Isotope in Sedimentary
1010 Geology. SEPM Short Course No. 10. Chapter 3. Dallas.
1011 Veizer, J., Clayton, R.N., Hinton, R.W., 1992. Geochemistry of Precambrian carbonates: IV. Early
1012 Paleoproterozoic (2.25 + 0.25 Ga) seawater. Geochim. Cosmochim. Acta 56, 875–885.
1013

Wigley, T.M.L., 1973a. Chemical evolution of the system calcite–gypsum–water. Canadian Journal of Earth Sciences 10, 306-314.

Wigley, T.M.L., 1973b. The incongruent solution of dolomite. Geochimica et Cosmochimica Acta 37, 1397-1402.

White, D.E., Brannock, W.W., Murata, K.J., 1956. Silica in hot-spring waters. Geochimica et Cosmochimica Acta 10, 27-59.

Yoshimura, K., Liu, Z., Cao, J., Yuan, D., Inokura, Y., Noto, M., 2004 Deep source CO2 in natural waters and its role in extensive tufa deposition in the Huanglong Ravines, Sichuan, China. Chemical Geology 205, 141-53.

Figure captions

Figure 1. (a) The location of the KSF and the Pechenga Greenstone Belt. (b) The location of Core 5A in the Pechenga Greenstone belt. Modified from Melezhik and Fallick (2005)

Figure 2. Lithostratigraphic profile of Core 5A (modified from Salminen et al., 2013a) and the C and O isotope composition of the surficial dolomite crusts and cements and carbonate fills in cavities and veins. The C and O isotope compositions of the host carbonates (micro-drilled samples; Salminen et al., 2013a) are shown for comparison. In addition, the estimated proportion of the carbonate crusts, cements and fills (Salminen et al., 2013a) is shown in the figure.

Figure 3. Cavities. (a) Dissolution cavity at the depth of 62.1 m. The cavity is mainly filled with dolospar. Dolostone immediately surrounding the cavity is recrystallized and has a powdery appearance. (b) Dissolution cavity at the depth of 69.6 m with complex internal structure. The outer zone of the cavity fill includes (1) thin laminae of dolomite and quartz (also forming “mounds”) and (2) yellowish sparitic calcite. These are sealed with (3) a thin rim of fibrous, inward-growing dolomite. Quartz with some dolomite and (4) pyrite represent the latest fills in the cavity.

Figure 4. Cavities. (a) Scanned image of a cavity at the depth of 83.0 m. The cavity is lined with several rims of sparitic dolomite, capped with a rim of fibrous dolomite. The remaining space is filled with dolospar and minor quartz. (b) Cavity (at the depth of 72.7 m) includes

quartz-filled fenestrae, some of them appearing as sulfate pseudomorphs (e.g. in the circled area).

Figure 5. Cavities with stalactites. (a) Quartz-filled and carbonate-walled cavity at the depth of 60.2 m. Note small white stalactites at the roof of the cavity. (b) Scanned slab showing gray-and-white, thinly-laminated crust (at the bottom) and stalactites in a cavity at a depth of 81.4 m. (c) Gray, white and yellow thinly-laminated dolomitic crust (at the bottom) and stalactites (in the middle), overlain by pinkish dolomite, at a depth of 31.4 m.

Figure 6. Veins. (a) A thin section showing a vein above a stromatolitic layer at the depth of 35.1 m. (b) A thin section showing a vein in sandy micritic dolostone at the depth of 62.7 m. (c) A probable burial vein in dolarenite overlying a sandstone-filled cavity (at the bottom). The vein shows coloration and mineralogical zoning. The innermost, reddish part is calcite. It is lined with a mixture of gray calcite and dolomite. The outermost white rim is composed of dolomite. The depth is 53.7 m.

Figure 7. A surficial dolomite crust at the depth of 68.3 m. (a) Thin-section of the crust. (b) Thin-section image of the crust (stereo microscope). The micritic/sparitic crust at the base (grayish color in the photo) shows upward growth and thin lamination. This part of the crust is overlain by a rim of fibrous dolomite (black colored in the photo). The entire crust is sealed with a silica sinter (bright colored in the photo) and overlain by a sandstone layer (at the top of the photo).

Figure 8. A probable surficial dolomite crust at 27.4 m. The crust is over- and underlain by sandy dolarenite. The basal part of the crust is composed of beige dolomitic bands overlain

by partially vuggy interval. The crust is capped with white rim of sparitic dolomite and a thin film of siliceous precipitate (a sinter or a silcrete). (a) A photo of the crust. (b) Scanned slab.

Figure 9. Dolomite cements. a) Scanned slab showing dolomite cement with feathery crystals, forming a mound-like structure at the depth of 76.4 m. b) Dolomite cements in a thin section. Fibrous dolomite cement forms thin crusts/mounds at the depth of 76.0 m. c) A thin section image of feathery dolomite cements (stereo microscope) at the depth of 76.0 m. d) A thin section image showing surficial cement (stereo microscope) at the depth of 76.9 m.

Figure 10. Acid-soluble elemental contents (ICP-MS) of the carbonate fills, cements and crusts. The elemental contents of the host carbonates (micro-drilled samples) have been adopted from Salminen et al. (2013a); the Ba contents for the host rocks have not been published.

Figure 11. Cross-plots of selected variables in carbonate fills, crusts and cements.

Figure 12. The C and O isotope composition and acid-soluble elemental compositions of micro-drilled subsamples from the cavity at 79.6 m. The subsamples were obtained from the circular spots shown in the slabs photo aside. The width of the slabs is ca. 2.5 cm.

Figure 13. The C and O isotope composition and acid-soluble elemental compositions of micro-drilled subsamples from the cavity at 81.4 m. The subsamples were obtained from the circular spots shown in the slab photos aside. The width of the slabs is ca. 2.5 cm.

Figure 14. A $\delta^{13}C$-$\delta^{18}O$ cross-plot of the subsamples from the cavities at 79.6 and 81.4 m and the surficial dolomite crusts at 30.3 and 68.3 m.

Figure 15. The C and O isotope composition of the micro-drilled subsamples from a cavity at 83.0 m. The subsamples were micro-drilled from the circular spots shown in the slab photo aside. The width of the slab is ca. 2.5 cm.

Figure 16. The C and O isotope composition of the dolospar fill from the cavity at 62.1 m. The C and O isotope composition of the dolostone immediately over- and underlying the cavity is also shown in the figure. The subsamples were micro-drilled from the circular spots shown in the slab photo aside. The width of the slab is ca. 2.5 cm.

Figure 17. The C and O isotope composition of the subsamples from the surficial dolomite crust at 30.3 m. The subsamples were obtained from the circular spots shown in the slab photo aside. The subsamples A-C were also analyzed for the acid-soluble elemental composition (results not shown in this figure). The width of the slab is ca. 2.5 cm.

Figure 18. The C and O isotope composition of the subsamples from the surficial dolomite crust at 68.3 m. The subsamples were micro-drilled from the circular spots shown in the slab photo aside. The width of the slab is ca. 2.5 cm.

Innline Supplementary Figure 1. Dolomite crust at the depth of 30.3 m. The crust starts with reddish dolomitic bands overlain by beige dolomite bands (the lower half), then followed by a crust with clotted microfabrics (the upper half). The dolomite crust contains small vugs filled with white, gray or black sparitic dolomite. There are also reddish fills in the vugs. (a) A photo of the crust. (b) Scanned slab of the crust showing also position of the micro-drilled subsamples.

Inline Supplementary Figure 2. A secondary electron image showing possible sulfate pseudomorphs (not visible in a back-scatter image) in dolomite cement at the depth of 76.9 m.

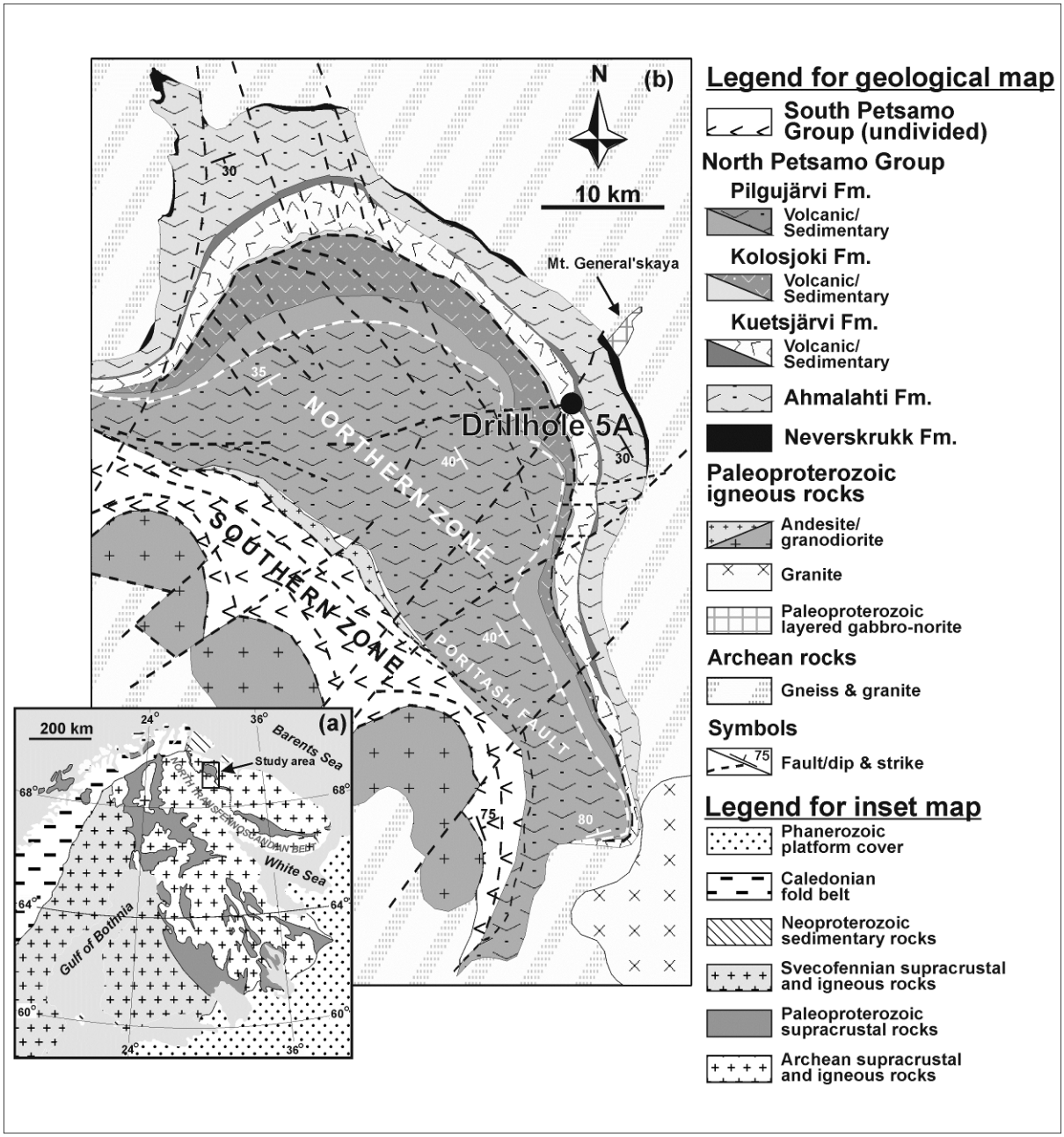
(b)
N
10 km
Mt. General'skaya
Drillhole 5A
NORTHERN ZONE
SOUTHERN ZONE
PORTAHASH FAULT
30
35
40
75
80
(a)
200 km
Study area
Barents Sea
White Sea
Gulf of Bothnia
68°
64°
60°
24°
36°
Legend for geological map
South Petsamo Group (undivided)
North Petsamo Group
Pilgujärvi Fm.
Volcanic/ Sedimentary
Kolosjoki Fm.
Volcanic/ Sedimentary
Kuetsjärvi Fm.
Volcanic/ Sedimentary
Ahmalahti Fm.
Neverskrukk Fm.
Paleoproterozoic igneous rocks
Andesite/ granodiorite
Granite
Paleoproterozoic layered gabbro-norite
Archean rocks
Gneiss & granite
Symbols
75
Fault/dip & strike
Legend for inset map
Phanerozoic platform cover
Caledonian fold belt
Neoproterozoic sedimentary rocks
Svecofennian supracrustal and igneous rocks
Paleoproterozoic supracrustal rocks
Archean supracrustal and igneous rocks

1133

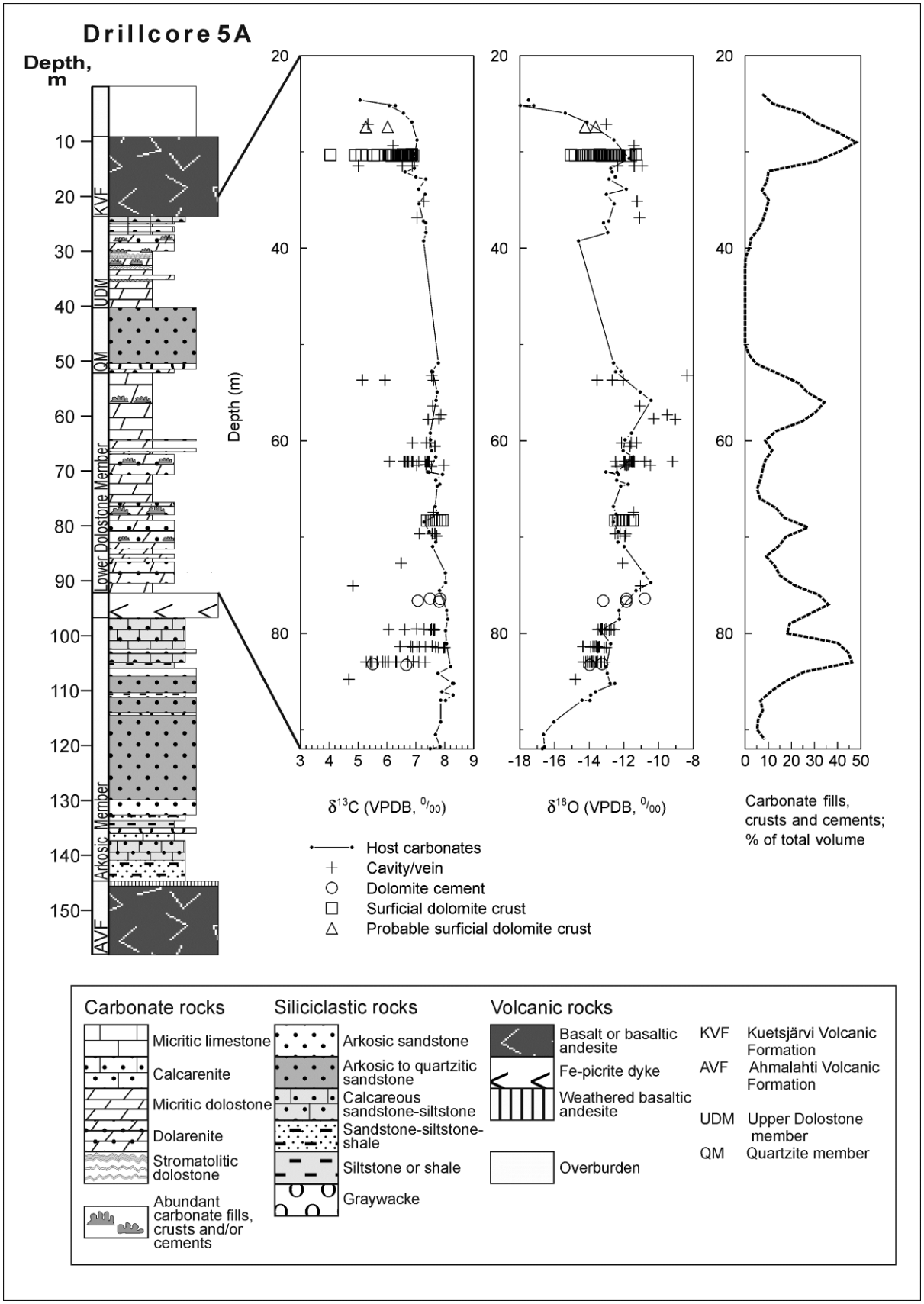
Drillcore 5A
Depth, m
KVF
UDM
QM
Lower Dolostone Member
Arkosic Member
AVF
Depth (m)
δ13C (VPDB, 0/00)
δ18O (VPDB, 0/00)
Carbonate fills, crusts and cements; % of total volume
Host carbonates
Cavity/vein
Dolomite cement
Surficial dolomite crust
Probable surficial dolomite crust
Carbonate rocks
Micritic limestone
Calcarenite
Micritic dolostone
Dolarenite
Stromatolitic dolostone
Abundant carbonate fills, crusts and/or cements
Siliciclastic rocks
Arkosic sandstone
Arkosic to quartzitic sandstone
Calcareous sandstone-siltstone
Sandstone-siltstone-shale
Siltstone or shale
Graywacke
Volcanic rocks
Basalt or basaltic andesite
Fe-picrite dyke
Weathered basaltic andesite
Overburden
KVF Kuetsjärvi Volcanic Formation
AVF Ahmalahti Volcanic Formation
UDM Upper Dolostone member
QM Quartzite member

1134

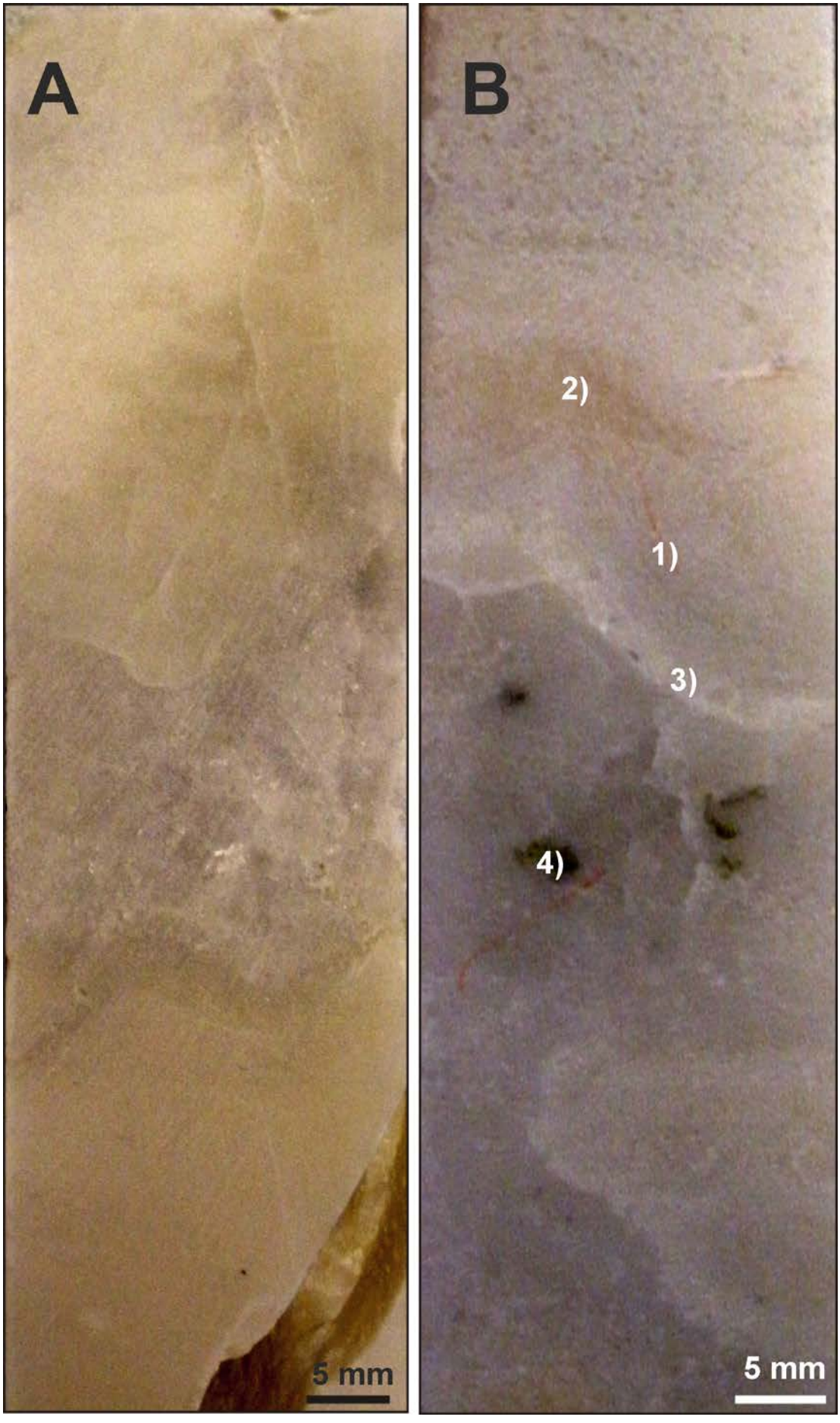

1135

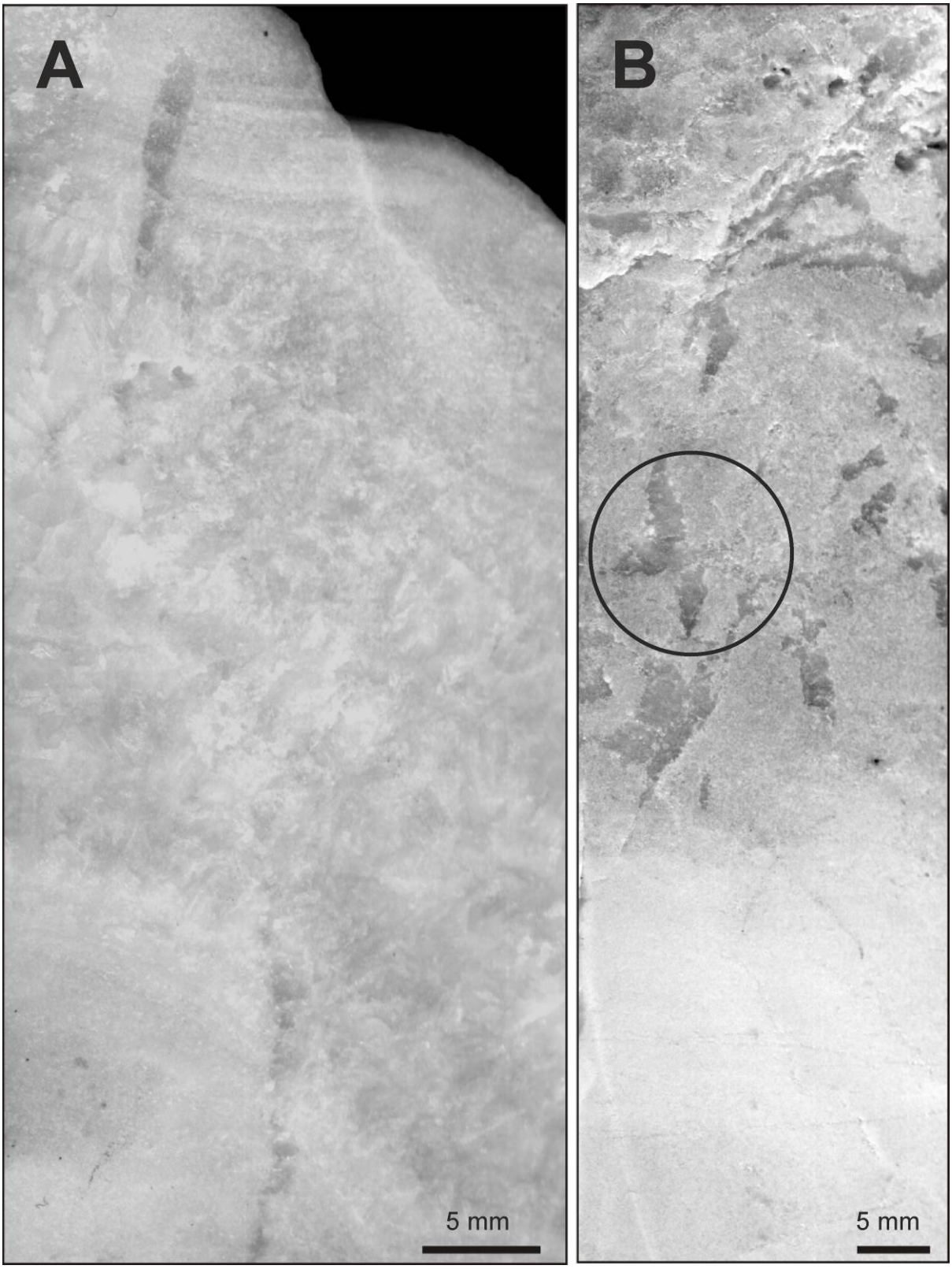

1136

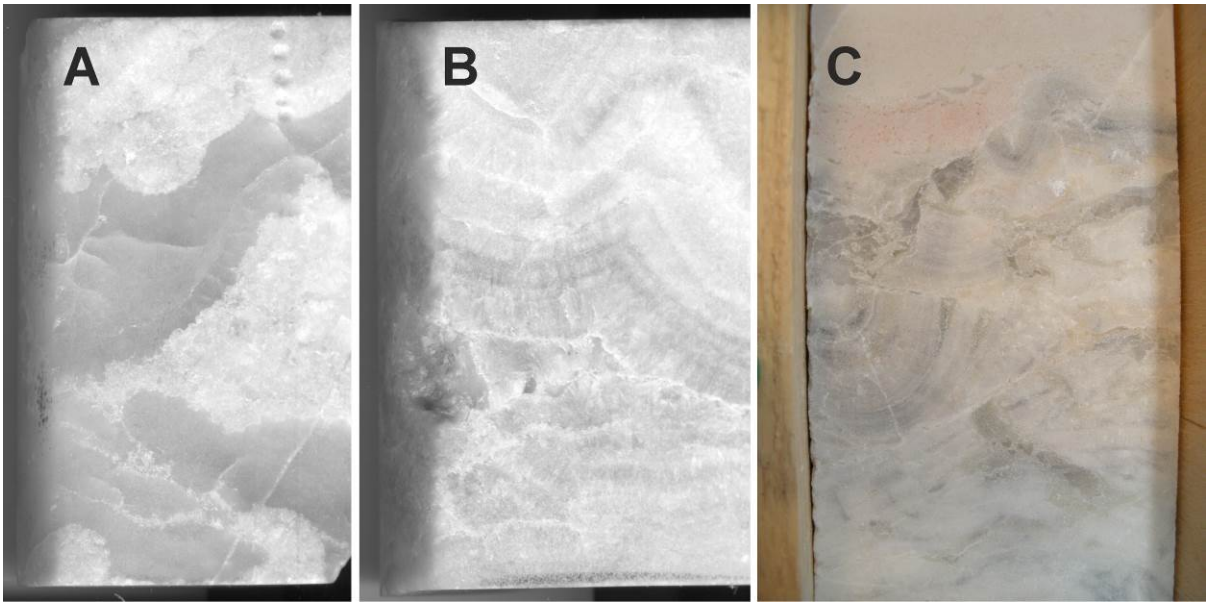

1137

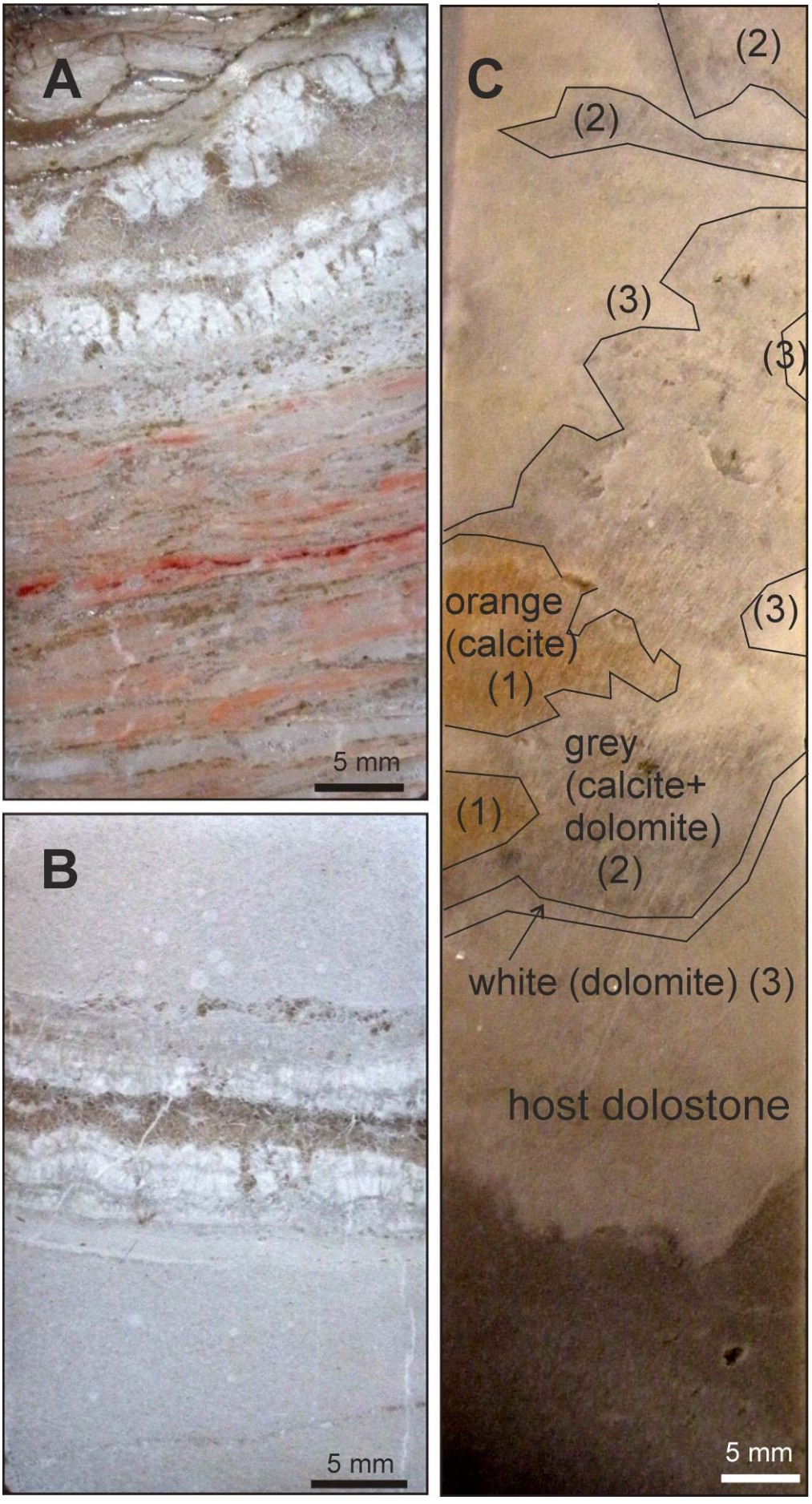
A
5 mm
B
5 mm
C
(2)
(2)
(3)
(3)
orange
(calcite)
(1)
(3)
grey
(calcite+
dolomite)
(2)
(1)
white (dolomite) (3)
host dolostone
5 mm

1138

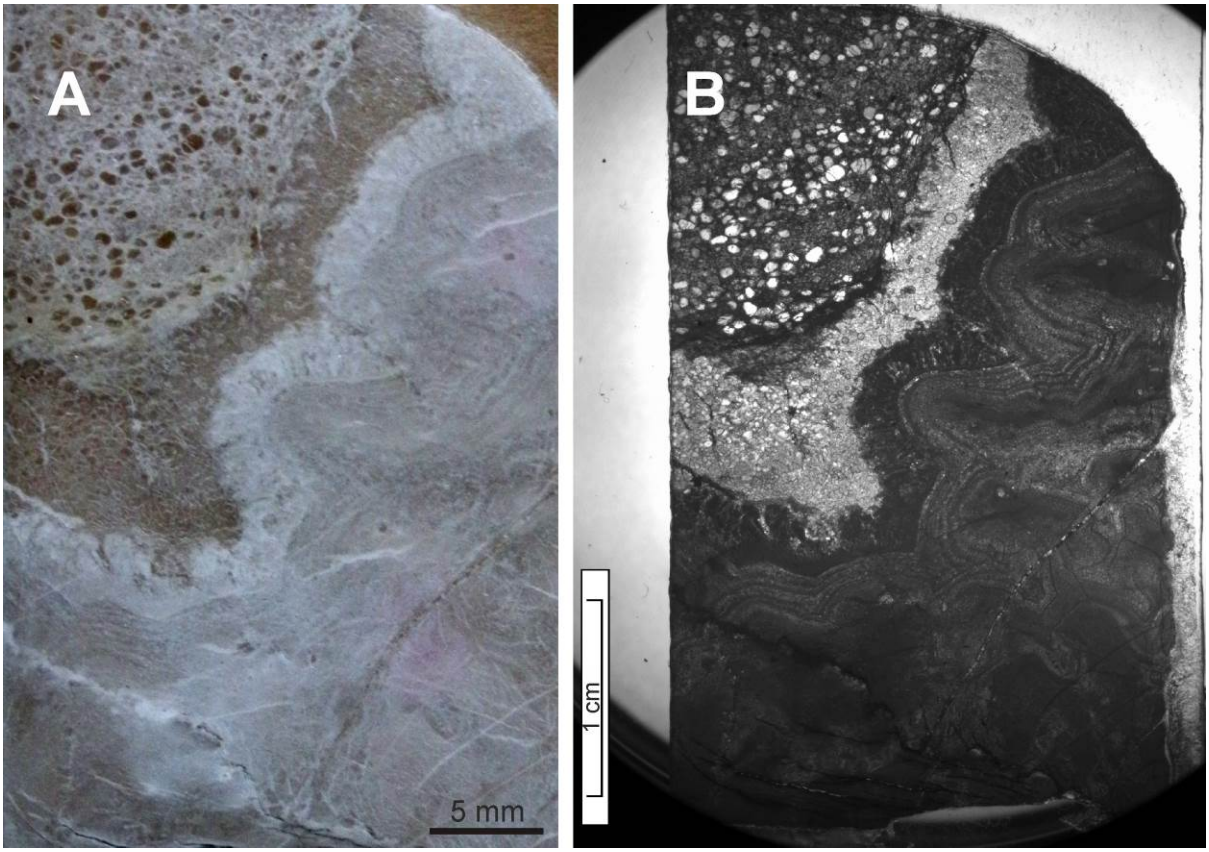

1139

1140

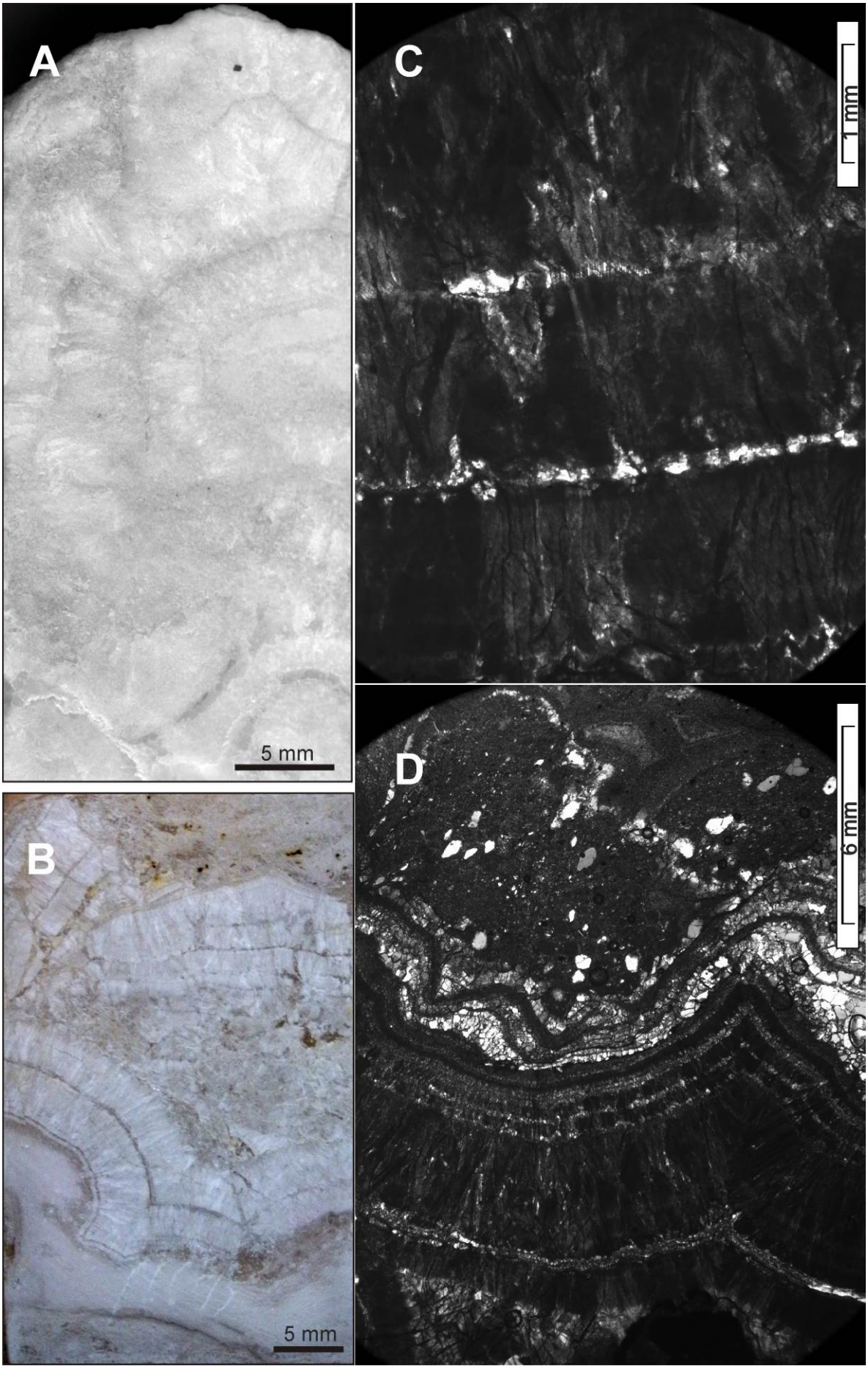

1141

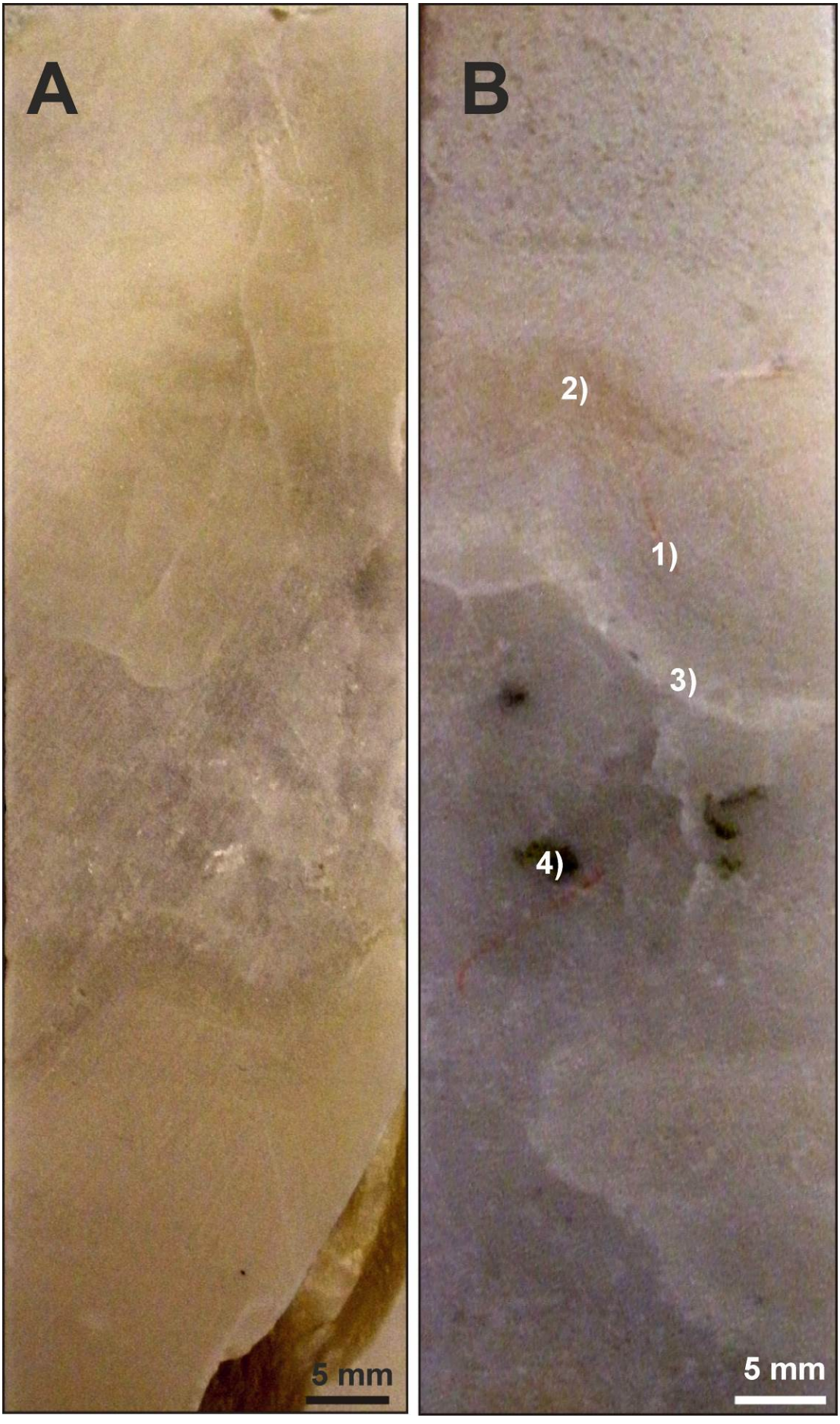

1142

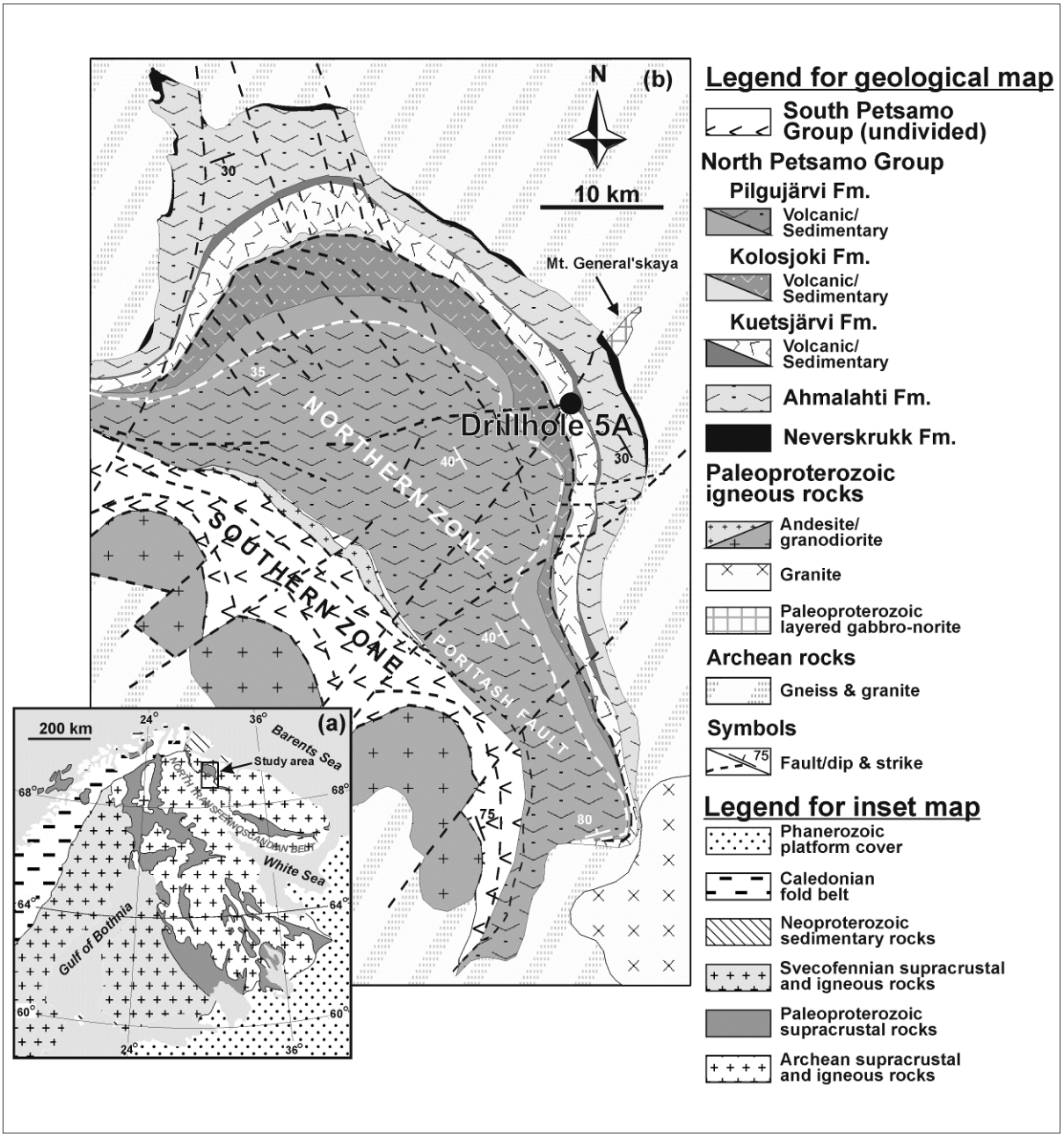
(b)
N
10 km
Mt. General'skaya
Drillhole 5A
NORTHERN ZONE
SOUTHERN ZONE
PORITASH FAULT
30
35
40
75
80
(a)
200 km
Barents Sea
Study area
White Sea
Gulf of Bothnia
68°
64°
60°
24°
36°
Legend for geological map
South Petsamo Group (undivided)
North Petsamo Group
Pilgujärvi Fm.
Volcanic/ Sedimentary
Kolosjoki Fm.
Volcanic/ Sedimentary
Kuetsjärvi Fm.
Volcanic/ Sedimentary
Ahmalahti Fm.
Neverskrukk Fm.
Paleoproterozoic igneous rocks
Andesite/ granodiorite
Granite
Paleoproterozoic layered gabbro-norite
Archean rocks
Gneiss & granite
Symbols
75
Fault/dip & strike
Legend for inset map
Phanerozoic platform cover
Caledonian fold belt
Neoproterozoic sedimentary rocks
Svecofennian supracrustal and igneous rocks
Paleoproterozoic supracrustal rocks
Archean supracrustal and igneous rocks

1143

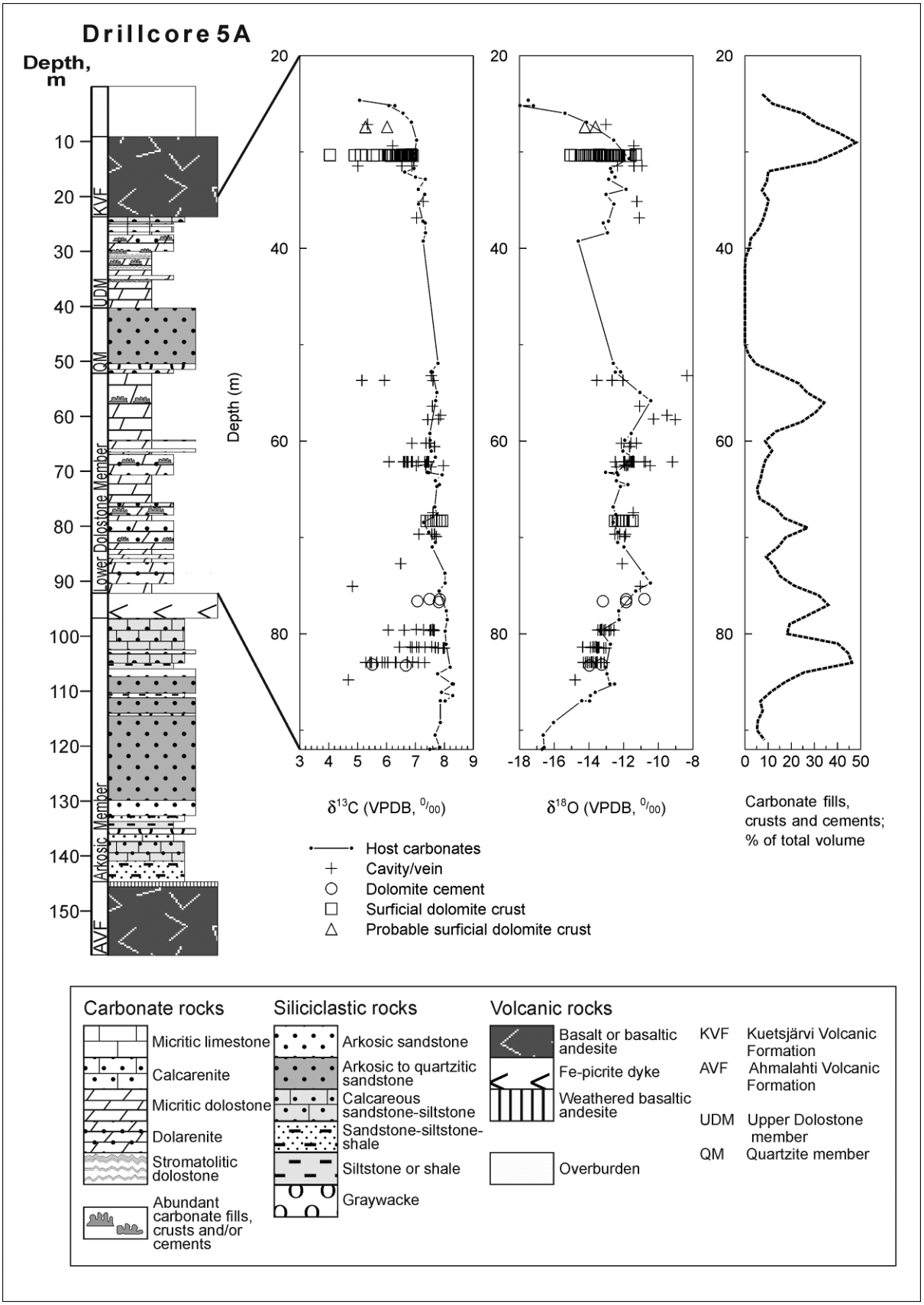
Drillcore 5A
Depth, m
KVF
UDM
QM
Lower Dolostone Member
Arkosic Member
AVF
Depth (m)
δ13C (VPDB, 0/00)
δ18O (VPDB, 0/00)
Carbonate fills, crusts and cements; % of total volume
Host carbonates
Cavity/vein
Dolomite cement
Surficial dolomite crust
Probable surficial dolomite crust
Carbonate rocks
Micritic limestone
Calcarenite
Micritic dolostone
Dolarenite
Stromatolitic dolostone
Abundant carbonate fills, crusts and/or cements
Siliciclastic rocks
Arkosic sandstone
Arkosic to quartzitic sandstone
Calcareous sandstone-siltstone
Sandstone-siltstone-shale
Siltstone or shale
Graywacke
Volcanic rocks
Basalt or basaltic andesite
Fe-picrite dyke
Weathered basaltic andesite
Overburden
KVF Kuetsjärvi Volcanic Formation
AVF Ahmalahti Volcanic Formation
UDM Upper Dolostone member
QM Quartzite member

1144

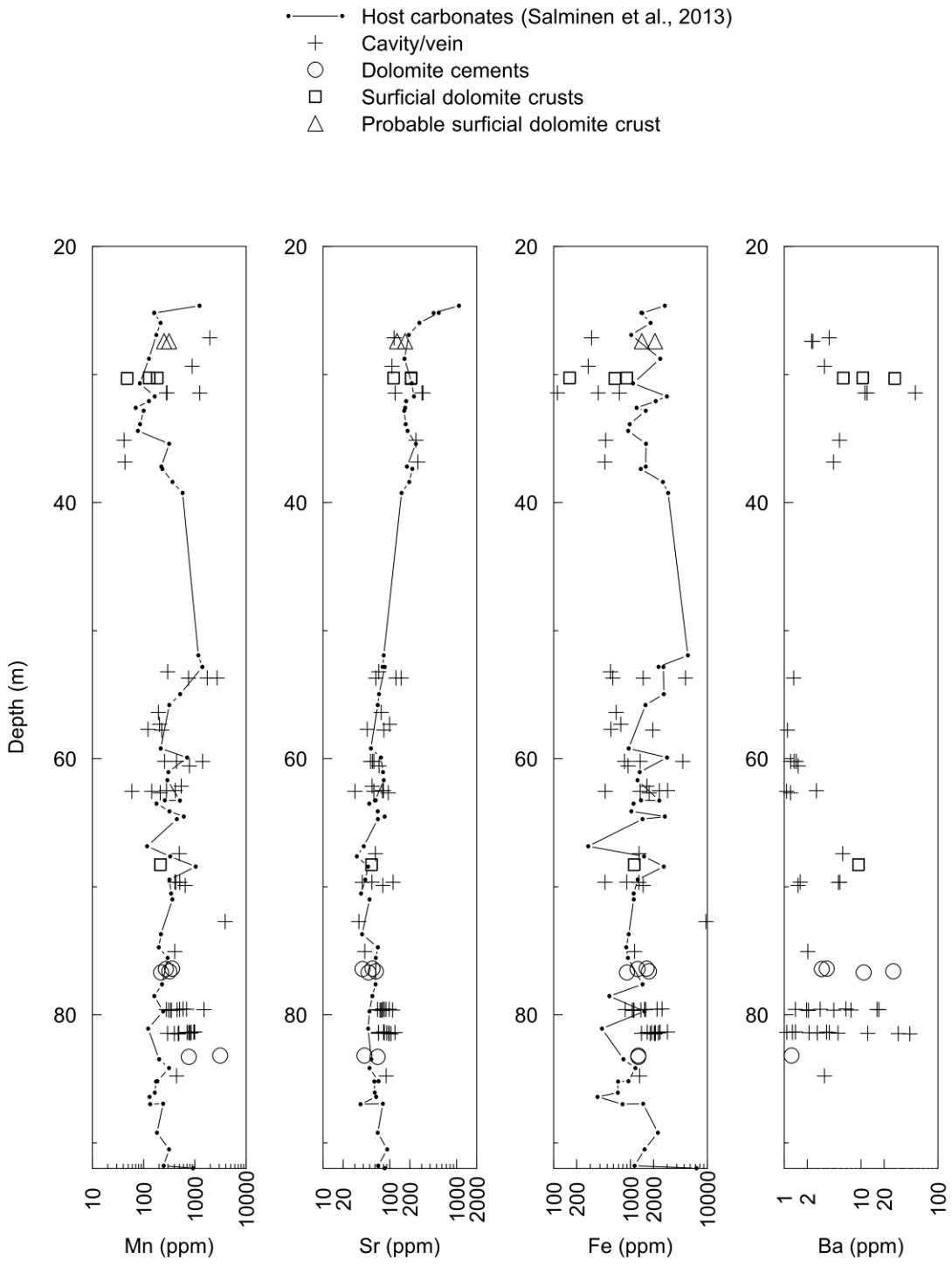
Host carbonates (Salminen et al., 2013)
Cavity/vein
Dolomite cements
Surficial dolomite crusts
Probable surficial dolomite crust
Depth (m)
20
40
60
80
10
100
1000
10000
Mn (ppm)
20
200
2000
Sr (ppm)
Fe (ppm)
1
2
Ba (ppm)

1145

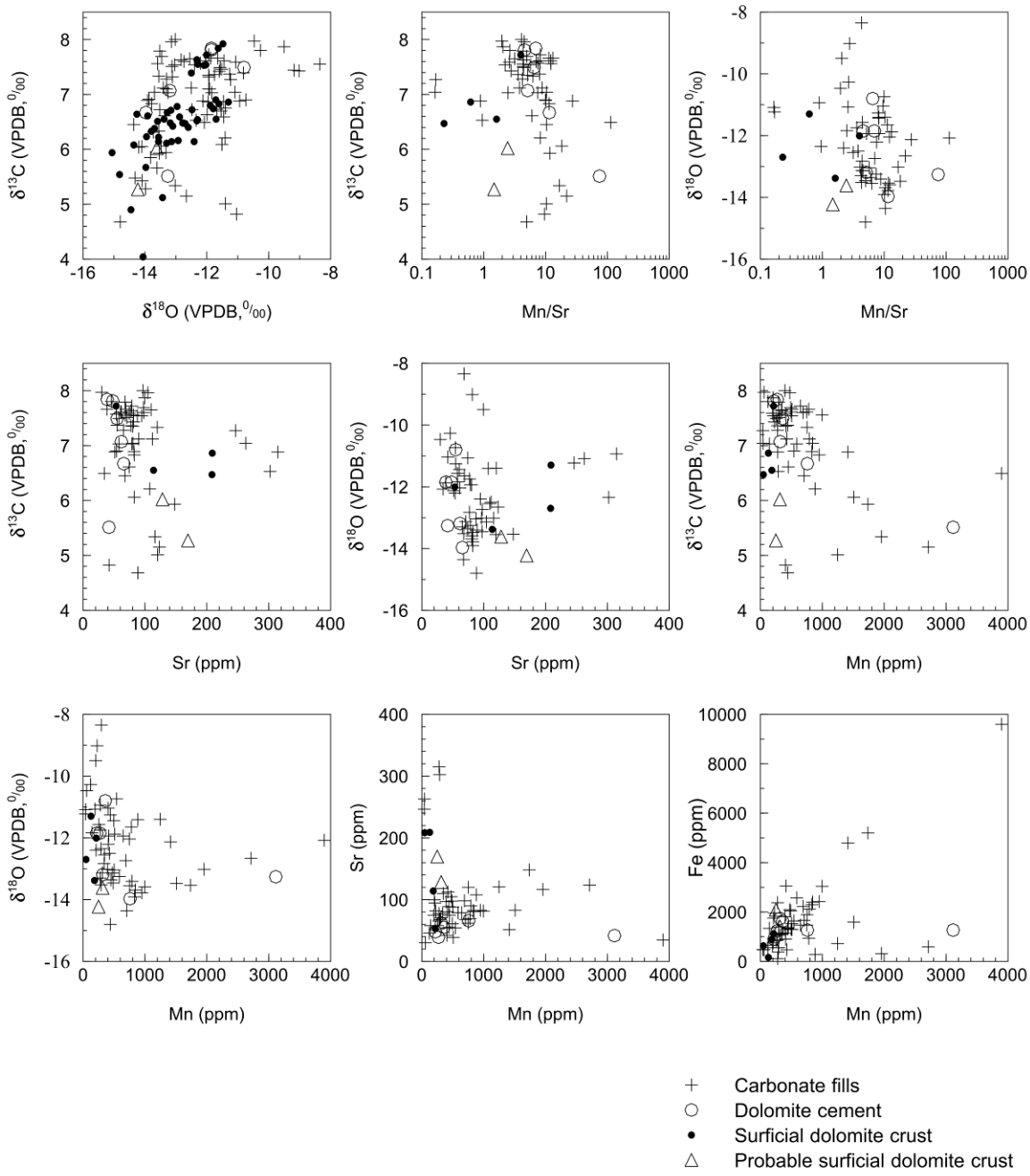
δ13C (VPDB,‰)
δ18O (VPDB,‰)
Mn/Sr
δ18O (VPDB,‰)
Mn/Sr
δ13C (VPDB,‰)
Sr (ppm)
δ18O (VPDB,‰)
Sr (ppm)
δ13C (VPDB,‰)
Mn (ppm)
δ18O (VPDB,‰)
Mn (ppm)
Sr (ppm)
Mn (ppm)
Fe (ppm)
Mn (ppm)
Carbonate fills
Dolomite cement
Surficial dolomite crust
Probable surficial dolomite crust

1146

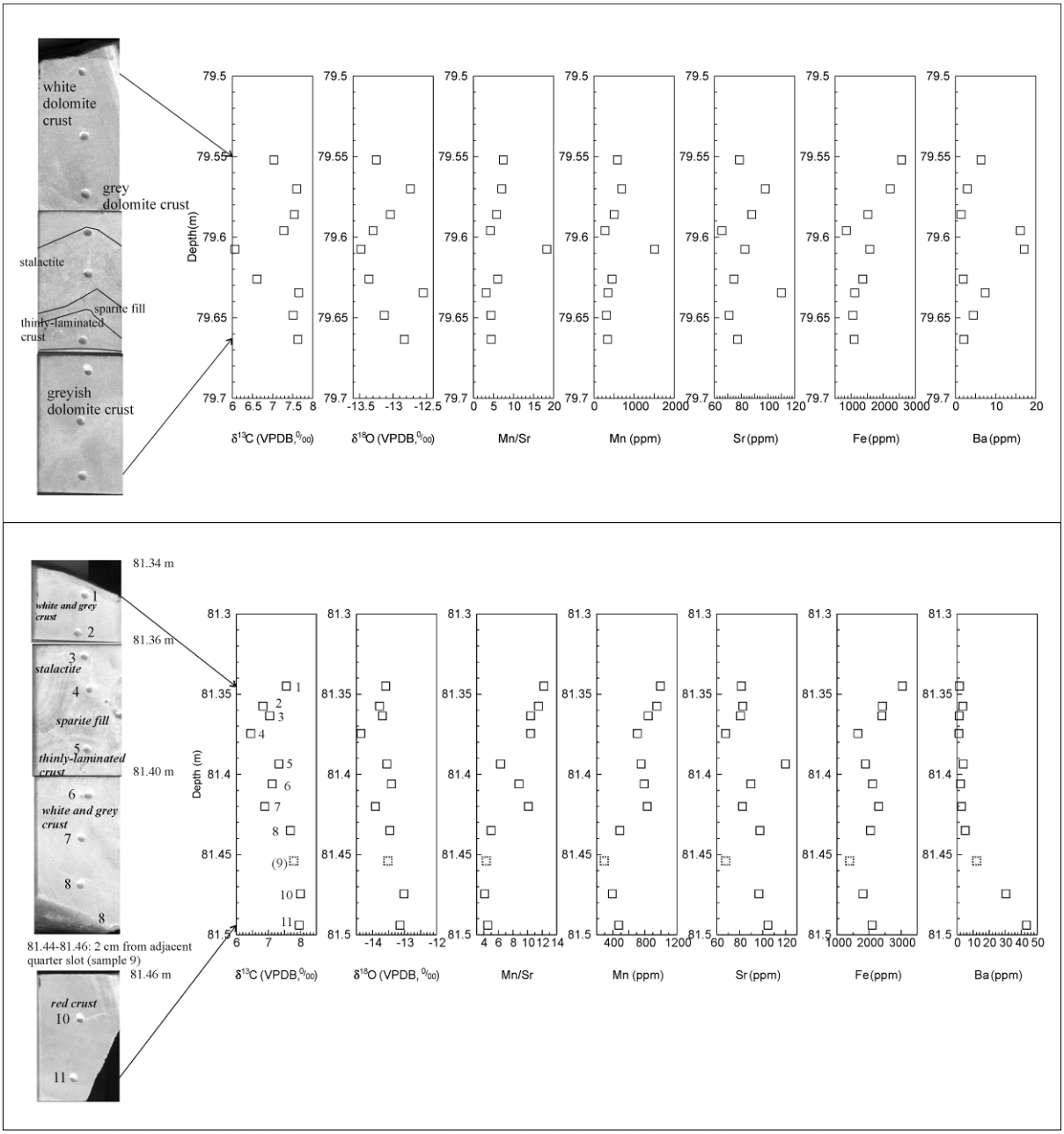
white dolomite crust
grey dolomite crust
stalactite
sparite fill
thinly-laminated crust
greyish dolomite crust
Depth(m)
δ13C (VPDB,‰)
δ18O (VPDB,‰)
Mn/Sr
Mn (ppm)
Sr (ppm)
Fe (ppm)
Ba (ppm)
81.34 m
81.36 m
81.40 m
81.44-81.46: 2 cm from adjacent quarter slot (sample 9)
81.46 m
white and grey crust
stalactite
sparite fill
thinly-laminated crust
white and grey crust
red crust
Depth (m)

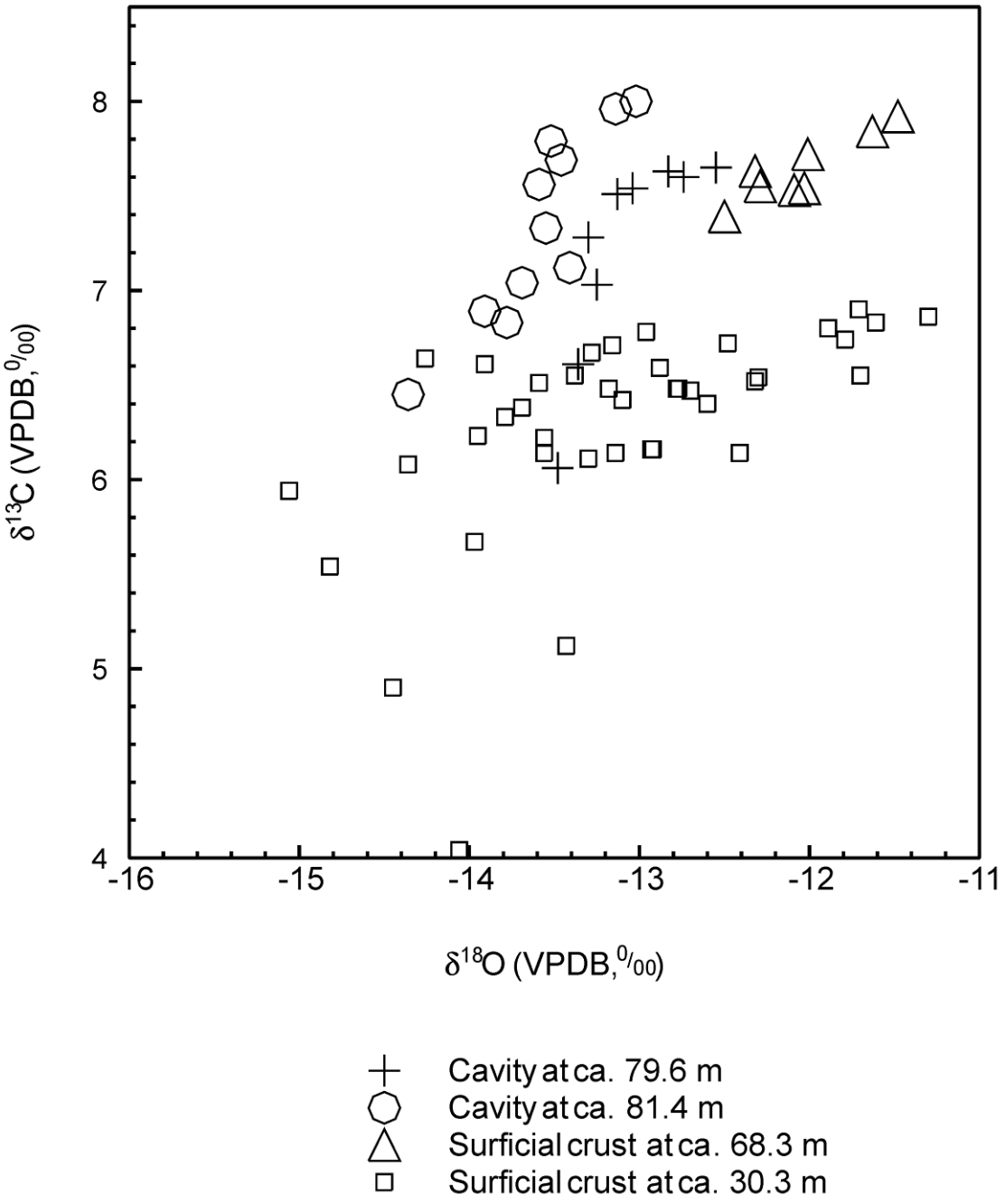
8
7
6
5
4
-16
-15
-14
-13
-12
-11
δ13C (VPDB,‰)
δ18O (VPDB,‰)
Cavity at ca. 79.6 m
Cavity at ca. 81.4 m
Surficial crust at ca. 68.3 m
Surficial crust at ca. 30.3 m

1149

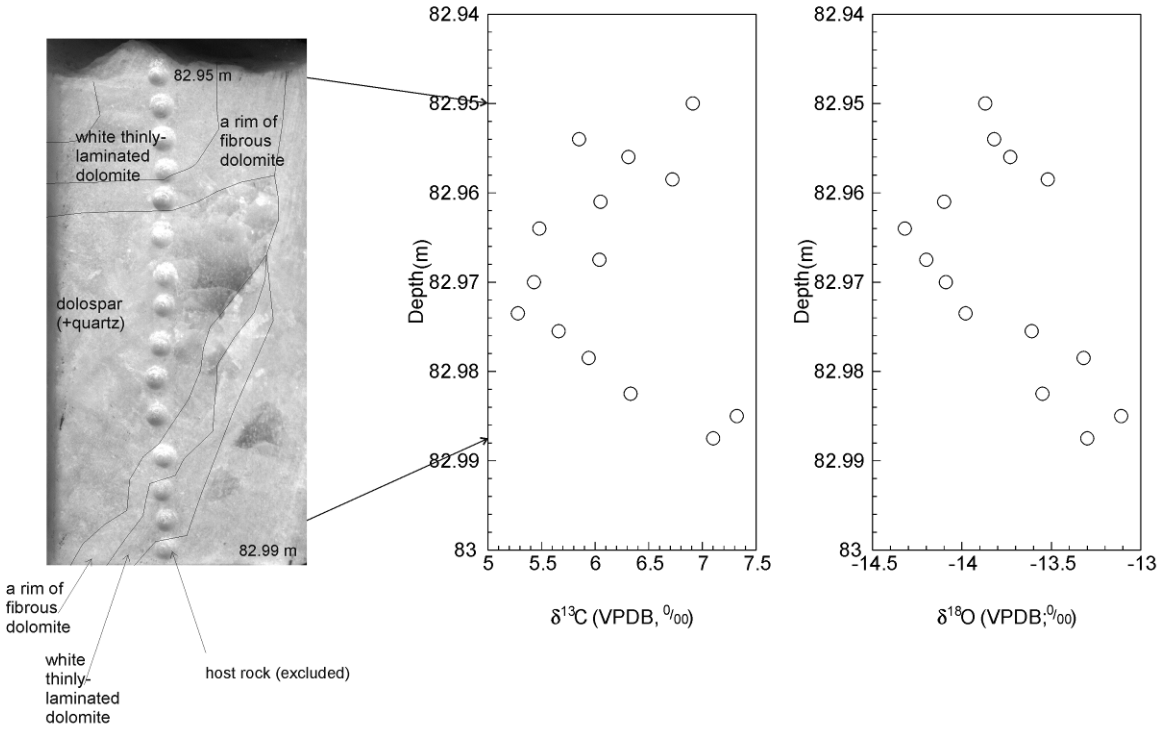
82.95 m
white thinly-laminated dolomite
a rim of fibrous dolomite
dolospar (+quartz)
82.99 m
a rim of fibrous dolomite
white thinly-laminated dolomite
host rock (excluded)
Depth(m)
82.94
82.95
82.96
82.97
82.98
82.99
83
5
5.5
6
6.5
7
7.5
δ13C (VPDB, 0/00)
-14.5
-14
-13.5
-13
δ18O (VPDB;0/00)

1150

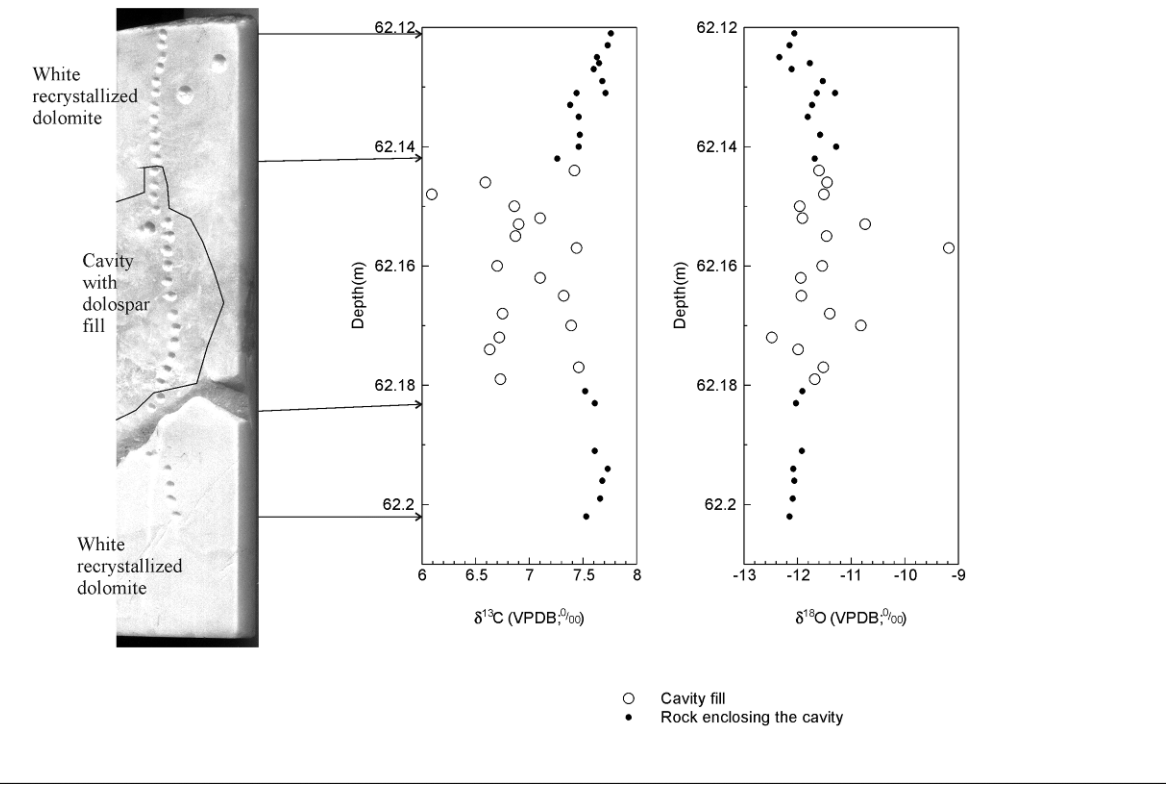
White recrystallized dolomite
Cavity with dolospar fill
White recrystallized dolomite
Depth(m)
62.12
62.14
62.16
62.18
62.2
6
6.5
7
7.5
8
δ13C (VPDB,0/00)
-13
-12
-11
-10
-9
δ18O (VPDB,0/00)
Cavity fill
Rock enclosing the cavity

1151

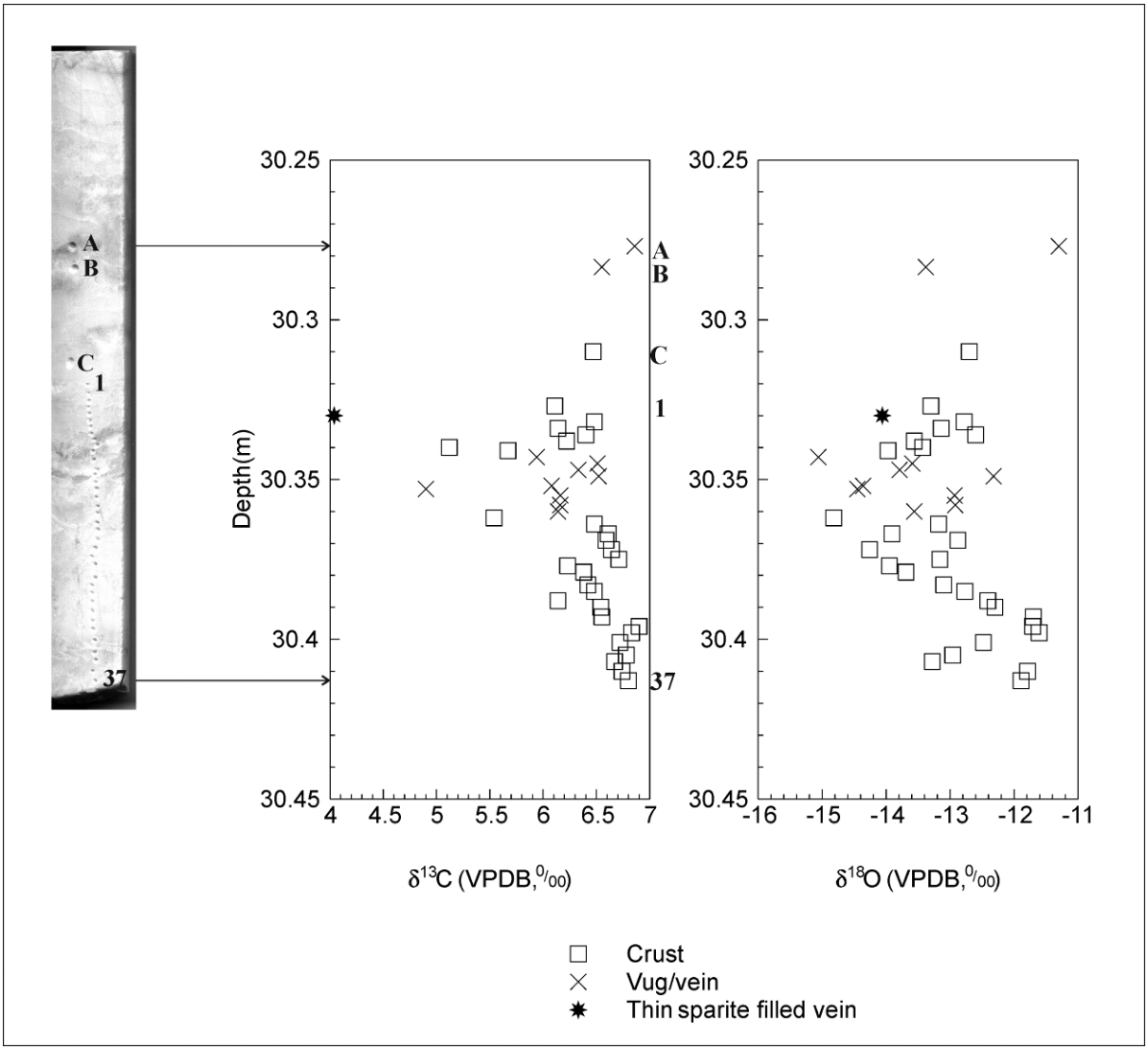
A
B
C
1
37
30.25
30.3
30.35
30.4
30.45
Depth(m)
4
4.5
5
5.5
6
6.5
7
δ13C (VPDB,0/00)
-16
-15
-14
-13
-12
-11
δ18O (VPDB,0/00)
Crust
Vug/vein
Thin sparite filled vein

1152

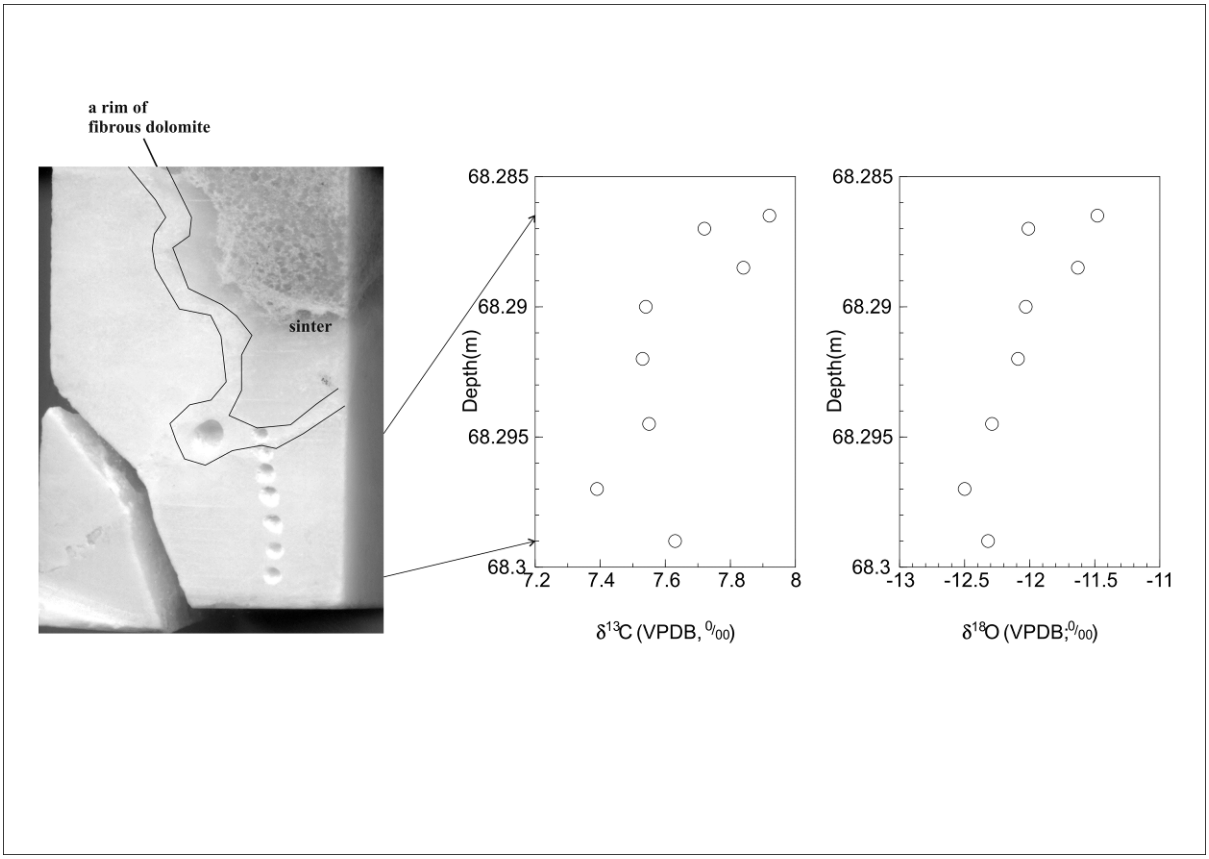
a rim of
fibrous dolomite
sinter
68.285
68.29
68.295
68.3
Depth(m)
7.2
7.4
7.6
7.8
8
δ13C (VPDB, 0/00)
68.285
68.29
68.295
68.3
Depth(m)
-13
-12.5
-12
-11.5
-11
δ18O (VPDB;0/00)

1153

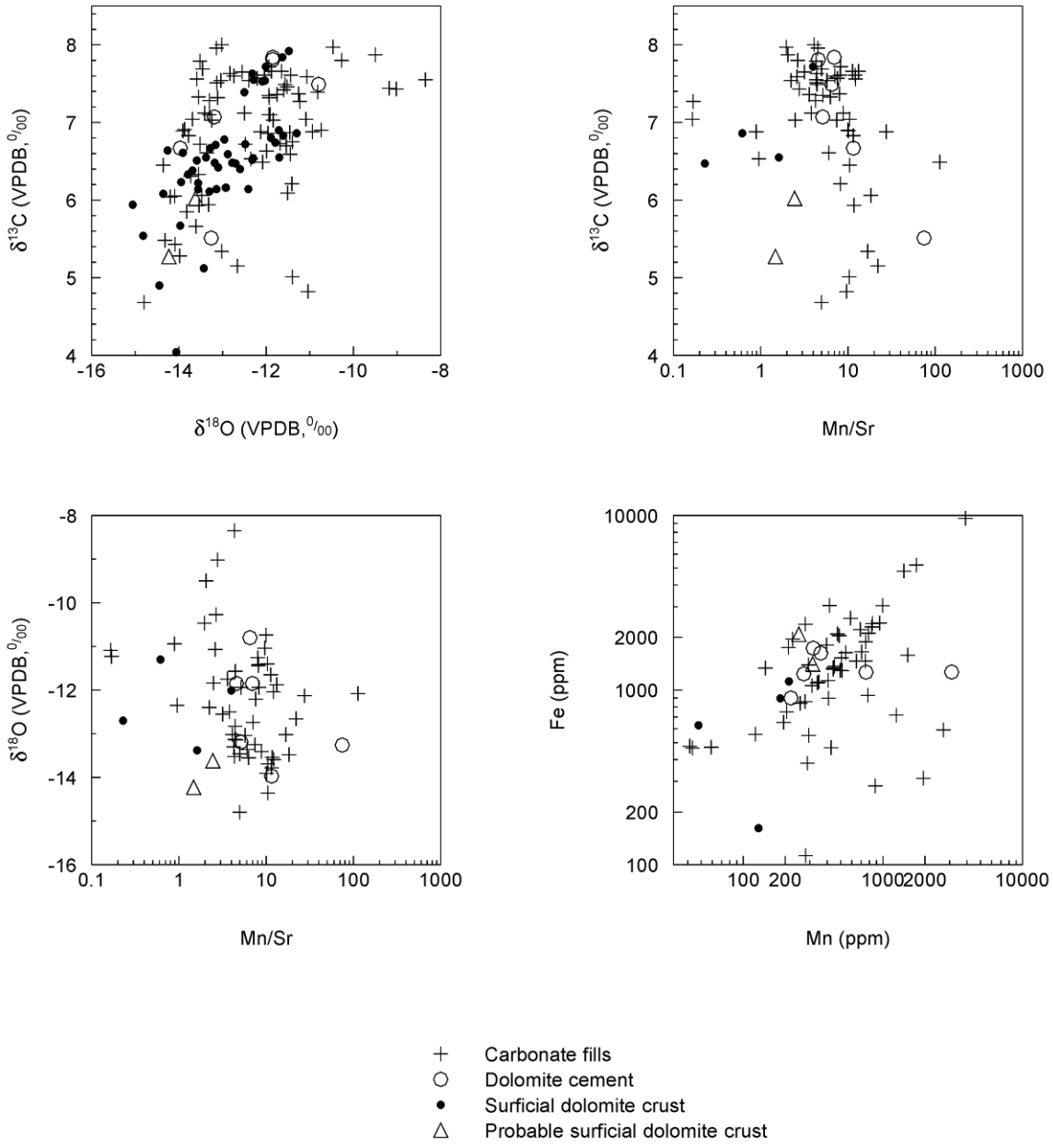
δ13C (VPDB, 0/00)
δ18O (VPDB, 0/00)
Mn/Sr
δ18O (VPDB, 0/00)
Mn/Sr
Fe (ppm)
Mn (ppm)
Carbonate fills
Dolomite cement
Surficial dolomite crust
Probable surficial dolomite crust

1154

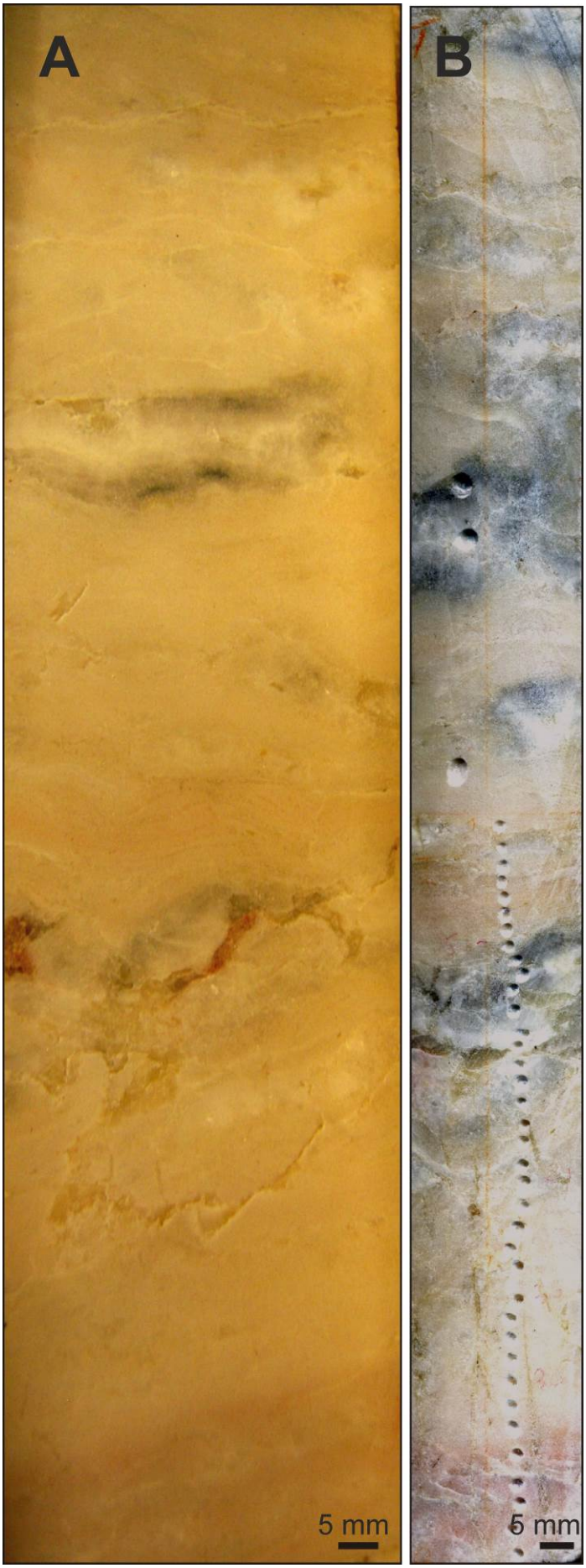

1155

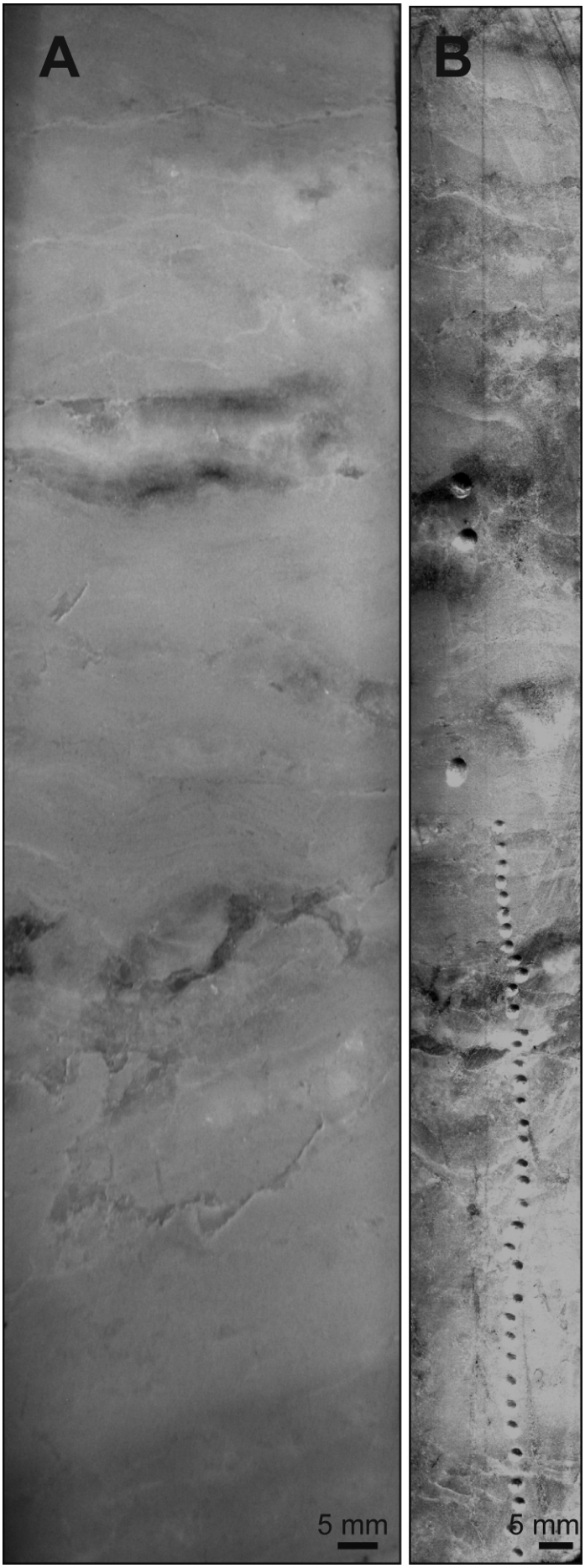

1156

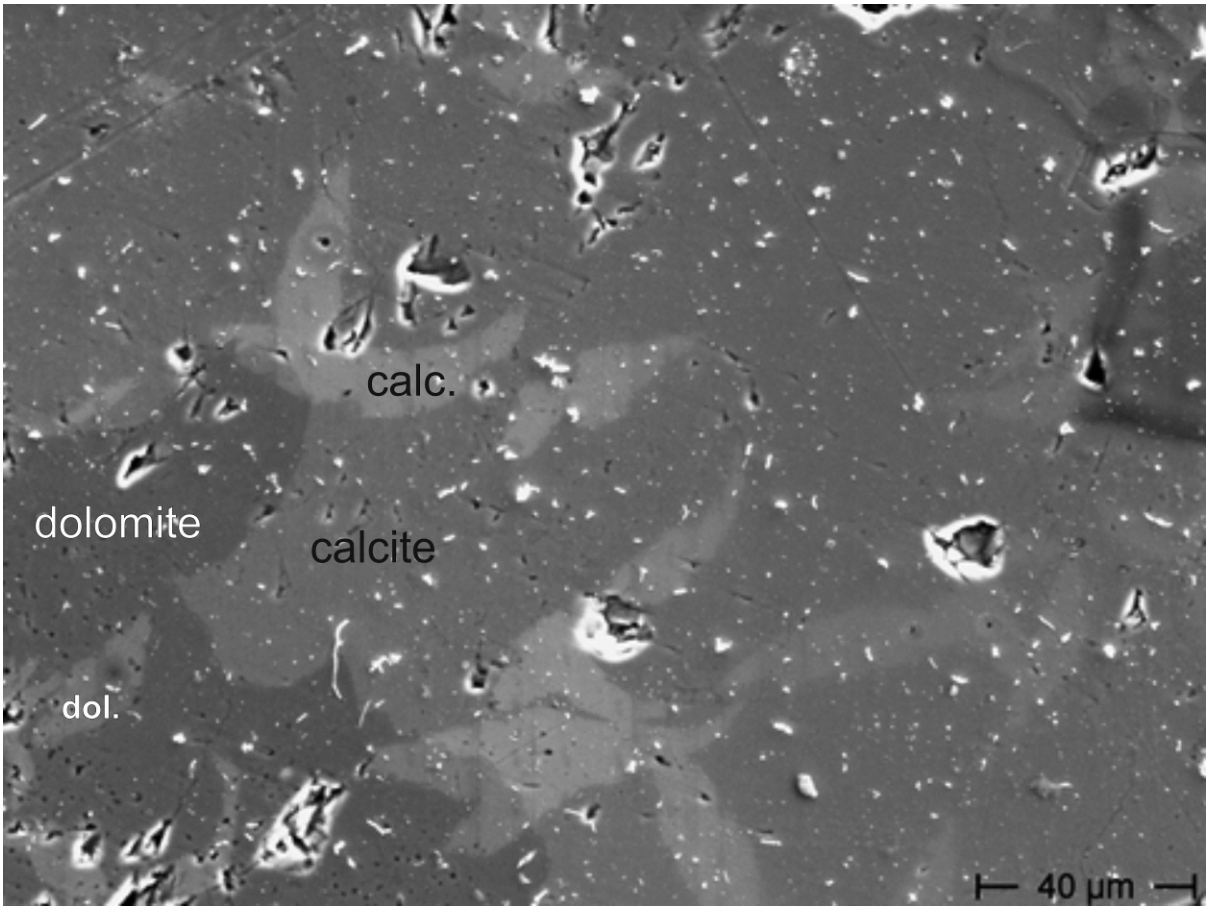

1157